New Journal of Physics
The open access journal at the forefront of physics

Deutsche Physikalische Gesellschaft DPG IOP Institute of Physics

PAPER • OPEN ACCESS

Bistability and oscillations in cooperative microtubule and kinetochore dynamics in the mitotic spindle

To cite this article: Felix Schwietert and Jan Kierfeld 2020 *New J. Phys.* **22** 053008

New Journal of Physics
The open access journal at the forefront of physics

Deutsche Physikalische Gesellschaft DPG
IOP Institute of Physics

Published in partnership with: Deutsche Physikalische Gesellschaft and the Institute of Physics

OPEN ACCESS

RECEIVED
6 December 2019

REVISED
5 March 2020

ACCEPTED FOR PUBLICATION
11 March 2020

PUBLISHED
1 May 2020

PAPER

Bistability and oscillations in cooperative microtubule and kinetochore dynamics in the mitotic spindle

Felix Schwietert and Jan Kierfeld[1]

Physics Department, TU Dortmund University, 44221 Dortmund, Germany
[1] Author to whom any correspondence should be addressed.

E-mail: jan.kierfeld@tu-dortmund.de

Keywords: mitotic spindle, directional instability, microtubule dynamics, kinetochore oscillations, bistability, stochastic simulation

Supplementary material for this article is available online

Abstract

In the mitotic spindle microtubules attach to kinetochores via catch bonds during metaphase, and microtubule depolymerization forces give rise to stochastic chromosome oscillations. We investigate the cooperative stochastic microtubule dynamics in spindle models consisting of ensembles of parallel microtubules, which attach to a kinetochore via elastic linkers. We include the dynamic instability of microtubules and forces on microtubules and kinetochores from elastic linkers. A one-sided model, where an external force acts on the kinetochore is solved analytically employing a mean-field approach based on Fokker–Planck equations. The solution establishes a bistable force–velocity relation of the microtubule ensemble in agreement with stochastic simulations. We derive constraints on linker stiffness and microtubule number for bistability. The bistable force–velocity relation of the one-sided spindle model gives rise to oscillations in the two-sided model, which can explain stochastic chromosome oscillations in metaphase (directional instability). We derive constraints on linker stiffness and microtubule number for metaphase chromosome oscillations. Including poleward microtubule flux into the model we can provide an explanation for the experimentally observed suppression of chromosome oscillations in cells with high poleward flux velocities. Chromosome oscillations persist in the presence of polar ejection forces, however, with a reduced amplitude and a phase shift between sister kinetochores. Moreover, polar ejection forces are necessary to align the chromosomes at the spindle equator and stabilize an alternating oscillation pattern of the two kinetochores. Finally, we modify the model such that microtubules can only exert tensile forces on the kinetochore resulting in a tug-of-war between the two microtubule ensembles. Then, induced microtubule catastrophes after reaching the kinetochore are necessary to stimulate oscillations. The model can reproduce experimental results for kinetochore oscillations in PtK1 cells quantitatively.

1. Introduction

Proper separation of chromosomes during mitosis is essential for the maintenance of life and achieved by the mitotic spindle, which is composed of two microtubule (MT) asters anchored at the spindle poles. The spindle contains three types of MTs classified according to their function [1]: astral MTs interact with the cell membrane to position the spindle poles, interpolar MTs interact with MTs from the opposite pole to maintain spindle length, and, finally, kinetochore MTs link to the chromosomes via the kinetochores at the centromere and can apply pulling forces via the linkage. The MT–kinetochore bond is a catch bond [2], i.e. tightening under tension but the molecular nature of the MT–kinetochore link is not exactly known and a complete mechanistic understanding of the catch bond is missing [3, 4] but probably involves Aurora B [5]; the Ndc80 complexes and Dam1 (in yeast) are believed to play a major role in the MT–kinetochore link. One function of the spindle is to align the chromosomes in the metaphase plate at the spindle equator. It

Table 1. Overview of assumptions of models exhibiting stochastic chromosome oscillations. In the referred sections we discuss how poleward flux, PEFs and the absence of pushing forces affect kinetochore dynamics in the model used for this work.

Reference (year)	Linker model	Catch bonds	Equal force sharing	Force-dep. MT rescue/cat.	MT pushing forces	PEFs	Poleward MT flux
Joglekar [15] (2002)	Hill sleeve		No	No	No	Yes	No
Civelekoglu-Scholey [16] (2006)	Motor	No	No	Yes	Yes	Yes	Yes
Civelekoglu-Scholey [19] (2013)	Viscoelastic	Yes	No	Yes	No	Yes	No
Shtylla [17, 18] (2010)	Hill sleeve		Yes	No	Yes	Yes	No
Banigan [20] (2015)	Elastic	Yes	No	Yes	Yes	No	Yes
Klemm [21] (2018)	Permanent		Yes	Yes	Yes	No	No
This work	Elastic	Yes	No	Yes	Section 8	Section 7	Section 6

has been observed in several vertebrate cells that chromosomes do not rest during metaphase but exhibit oscillations along the pole to pole axis known as directional instability [6–12], whereas in Drosophila embryos and Xenopus eggs a directional instability does not occur [13, 14]. If present, these oscillations are stochastic and on the time scale of minutes, i.e., on a much larger time scale than the dynamic instability of single MTs. Both single kinetochores and the inter-kinetochore distance oscillate; inter-kinetochore or breathing oscillations occur with twice the frequency of single kinetochore oscillations [11].

A quantitative understanding of the underlying mechanics of the MT–kinetochore-chromosome system is still lacking. In the past, several theoretical models have been proposed that reproduce chromosome oscillations [15–21]. (See table 1 and reviews [22, 23].) These models have in common that they simplify to a quasi-one-dimensional geometry and contain two ensembles of MTs growing from the two spindle poles that connect to one chromosome that is represented by two kinetochores connected by a spring (the cohesin bond). Kinetochores follow overdamped motion [16–20] or are assumed to reach force balance instantaneously under the influence of MT depolymerization and polymerization forces (because the friction force is small) [15, 21].

Several MT depolymerization and polymerization forces are included into the models. The models neglect explicit spindle pole dynamics but possibly include poleward MT flux [16, 20], which describes a constant flux of tubulin from the plus-ends toward the spindle pole and is probably driven by plus-end directed kinesin-5 motors pushing overlapping antiparallel interpolar MTs apart and kinesin-13 proteins that depolymerize MTs at the centrosome [24]. The main poleward forces on kinetochores are generated by depolymerization of MTs which builds up and transmits a poleward force via the MT–kinetochore link. Only in the model of Civelekoglu-Scholey *et al* [16] the main poleward force is generated by MT depolymerization motors at the spindle poles. In order to be able to exert poleward pulling forces the MT–kinetochore bond needs to remain intact during depolymerization and 'slide' with the depolymerizing MT plus end. The force that can be exerted depends on the nature of this bond and is high if it is a catch bond that tightens under tension [2]. All models include switching between polymerizing and depolymerizing MT states; in most models this switching is caused by catastrophe and rescue events (dynamic instability [25]), only Shtylla and Keener [17, 18] do not introduce explicit MT catastrophes but catastrophe-like events are triggered by a chemical feedback loop if MTs approach the kinetochore.

The two ensembles of MTs are engaged in a kind of tug-of-war and exert antagonistic forces via the spring connecting kinetochores: poleward (P) depolymerization forces of one ensemble generate an antipoleward (AP) force on the other kinetochore. Experiments suggest that kinetochore MTs can only exert P-directed pulling forces by depolymerization but are not able to directly exert AP-directed pushing forces on the kinetochore during polymerization [7, 26]. During directional instability, the spindle switches between the left and the right ensemble pulling actively in P-direction by depolymerization while the respective other ensemble is passively following in AP-direction by polymerization without actively pushing. Nevertheless, some models have included AP-directed MT pushing forces [16–18, 20, 21]. Antagonistic AP-directed forces on the kinetochores can also be generated by polar ejection forces (PEFs); they originate from non-kinetochore MTs interacting with the chromosome arms via collisions or chromokinesins belonging to the kinesin-4 and kinesin-10 families [27] and pushing them thereby toward the spindle equator. The action of different P- and AP-directed forces can move kinetochores back and forth and also tense and relax the inter-kinetochore cohesin bond.

Models differ in their assumptions about the MT–kinetochore link and the mechanism how MT dynamics is directed by mechanical forces to give rise to kinetochore and inter-kinetochore distance oscillations. The model by Joglekar and Hunt [15] uses the thermodynamic Hill sleeve model [28] for the MT–kinetochore connection, which assumes equally spaced rigid linkers that diffuse on the discrete MT lattice. Shtylla and Keener [17, 18] combine a continuous version of the Hill sleeve model with a negative

chemical feedback between the force at the MT–kinetochore interface and the depolymerization rate. In Hill sleeve models there is no effect of MT insertion and, thus, force onto the MT dynamic instability, i.e., on catastrophe and rescue rates. The Hill sleeve can transmit pulling forces onto the kinetochore up to a critical force above which MTs pull out of the sleeve [15], and there is evidence that the Hill sleeve exhibits catch-bond-like behavior [29]. More recent studies show that the kinetochore is not rigid, as supposed in the Hill sleeve model, but should be viewed as a flexible framework [30]. Moreover, Ndc80 fibrils have been suggested as main force transmitter [4, 31, 32], which motivated Keener and Shtylla to modify their Hill sleeve model by replacing the rigid attachment sites with elastic linkers and allowing for a force feedback onto MT depolymerization [33]. However, sleeve models remain speculative as electron microscopy has not yet revealed appropriate structures [34, 35]. Civelekoglu-Scholey *et al* [16] proposed a model in which MTs and kinetochores are linked by motor proteins (dyneins) walking toward the MT minus end; these links have no catch-bond-like behavior. The links are assumed to be able to transmit tension onto MTs that promotes MT rescue. In [21] no explicit linkers are introduced but permanent MT–kinetochore links are assumed that can transmit both pulling and pushing forces onto MTs. As the exact nature of MT–kinetochore linking structures is not known, a model of the MT–kinetochore linkage as a generic elastic structure seems reasonable, as in recent models where the MTs are linked to the kinetochore via (visco-)elastic springs [19, 20]. The MT–kinetochore bond can be modeled as a catch bond, and the elastic linkers also transmit forces back onto the MT allowing for a force feedback onto MT dynamics as it has been measured in [2].

In the model of Shtylla and Keener [17], MTs that are attached to the same kinetochore share the force from the cohesin bond equally and exhibit synchronous dynamics. The last assumption is contradictory to the experimental observation that one kinetochore MT ensemble does not coherently (de)polymerize but always consists of a mixture of both states [36, 37]. Klemm *et al* [21] take into account this observation by dividing each MT ensemble into a growing and a shrinking sub-ensemble, but also make the strong assumption of equal force sharing between the MTs within each sub-ensemble. All other models allow for individual MT dynamics and for different forces between MTs depending on the distances of MTs to the kinetochore.

The main mechanism for oscillations differs between models depending on the main antagonistic AP-directed force that switches a depolymerizing P-directed ensemble back into AP-directed polymerization. Switching can be triggered by the AP-directed force that the other ensemble can exert via the cohesin spring during depolymerization and by AP-directed PEFs if MT catastrophes are suppressed or rescues promoted under tension. In the model by Joglekar and Hunt [15] AP-directed PEFs are essential for switching. Civelekoglu-Scholey *et al* [16] proposed a model in which force is transmitted by motor proteins. By variation of the model parameters they were able to reproduce a wide range of chromosome behavior observed in different cell types. In this model, a depolymerizing P-directed ensemble switches because tension in the cohesin spring and PEFs promote rescue events. A modified model [19] uses viscoelastic catch bonds and accounts for the observation that in PtK1 cells only chromosomes in the center of the metaphase plate exhibit directional instability [11]. They explain this dichotomy with different distributions of PEFs at the center and the periphery of the metaphase plate. In the model by Shtylla and Keener [17, 18] MT catastrophe-like events are only triggered by a chemical feedback such that kinetochore oscillations become coupled to oscillations of the chemical negative feedback system: AP-directed MT polymerization exerts pushing forces onto the kinetochore but triggers switching into a depolymerizing state, and MT depolymerization exerts P-directed pulling forces and triggers switching back into a polymerizing state.

Whereas in [15, 16, 19] AP-directed PEFs are present and in the model by Joglekar and Hunt [15] also essential for realistic kinetochore oscillations, Banigan *et al* [20] presented a minimal model with simple elastic linkers and neglecting PEFs. Referring to experiments with budding yeast kinetochores [2], they modeled MT dynamics with force-dependent velocities, catastrophe and rescue rates. In this model, kinetochore oscillations arise solely from the collective behavior of attached MTs under force and the resulting interplay between P-directed depolymerization forces and AP-directed polymerization forces of the opposing MT ensembles. Force-dependent velocities, catastrophe and rescue rates are essential to trigger switching of kinetochore motion and oscillations in this model. MTs can exert pushing forces such that it is unclear to what extent the oscillation mechanism remains functional if pushing forces are absent as suggested experimentally. Also the recent model by Klemm *et al* [21], which aims to describe kinetochore dynamics in fission yeast, does not rely on PEFs. It uses a permanent MT–kinetochore bond and oscillations result from the interplay between MT depolymerization and polymerization forces via force-dependence in MT dynamics; also in this model MTs can exert pushing forces. Moreover, the model makes the strong assumption of equal force sharing between all growing or shrinking MTs attached to a kinetochore. The model also includes kinesin-8 motors that enhance the catastrophe rate and have a centering effect on the chromosome positions.

In all references [15–21] a sufficient set of ingredients is given for the respective model to exhibit oscillations including a specific choice of parameter values. It is much harder to give necessary conditions and parameter ranges for oscillations, which means to obtain quantitative bounds on model parameters, than to give a sufficient set of conditions. This is the aim of the present paper within a model that starts from the minimal model by Banigan *et al* and generalizes this model in several respects in later sections, see table 1. In this way we discuss the complete inventory of possible forces acting on the kinetochore and its influence on oscillations.

It is also difficult to trace the actual mechanism leading to oscillations. An essential part in our quantitative analysis is a mean-field solution of the one-sided minimal model of Banigan *et al* [20], where a single kinetochore under force is connected to one or several MTs that experience length-dependent individual loads and feature force-dependent dynamics. Force–velocity relations for a single kinetochore, which is connected to one or several MTs have been investigated previously based on a sleeve-like MT–kinetochore interface [17, 18, 29, 33]. Here, we can derive an analytical solution of the one-sided minimal model from a novel mean-field approach. For this purpose, we start from the Fokker–Planck equations for the length distribution of the MT–kinetochore linkers. The only mean-field approximation is to neglect stochastic velocity fluctuations of the attached kinetochore. Our solution clearly shows that the force feedback of linkers onto the MT depolymerization dynamics via catch (or permanent) bonds is essential for a bistable force–velocity relation within the minimal model. Moreover, the stationary state solution allows us to quantify the parameter range for a bistability in the parameter plane of MT–kinetochore linker stiffness and MT numbers.

By interpreting the force–velocity relation as phase space diagram for the two-sided model as in [20], we show that bistability in the one-sided model is a necessary condition for kinetochore oscillations in the two-sided model. Beyond that, we are able (1) to quantify an oscillatory regime, in which kinetochores exhibit directional instability, in the parameter plane of linker stiffness and MT numbers predicting that linkers have to be sufficiently stiff; (2) to describe kinetochore motion in this oscillatory regime, calculate frequencies which agree with *in vivo* measurements [11] and to explain frequency doubling of breathing compared to single kinetochore oscillations; (3) to describe kinetochore motion in the non-oscillatory regime as fluctuations around a fixed point; (4) to show that high poleward flux velocities move the system out of the oscillatory regime and thereby explain why directional instability has been observed in mitotic vertebrate cells but not in Drosophila embryos and Xenopus eggs; (5) to show that polar ejection forces reduce the amplitude of oscillations, induce a phase shift between sister kinetochores and are necessary to align the chromosome at the spindle equator; (6) to derive as necessary condition for oscillations that either MTs must be able to apply pushing forces on the kinetochore or a catastrophe has to be induced with increased catastrophe rate when a MT reaches the kinetochore (7) to provide a set of model parameters that reproduce experimental results for kinetochore oscillations in PtK1 cells quantitatively. All these results are validated by stochastic simulations.

In particular, we quantify lower bounds for linker stiffnesses that allow oscillations, whose value depends on the behavior of MTs growing against the kinetochore. If kinetochore MTs can exert pushing forces, we find oscillations for linker stiffnesses >16 pN μm^{-1}; also if MT catastrophes are induced upon reaching the kinetochore, we find oscillations in a similar range of linker stiffnesses. These constraints provide useful additional information on MT–kinetochore linkers whose molecular nature is not completely unraveled up to now.

2. Mitotic spindle model

We use a one-dimensional model of the mitotic spindle (figure 1(a)), similar to the model from [20]. The x-coordinate specifies positions along the one-dimensional model, and we choose $x = 0$ to be the spindle equator. The spindle model contains a single chromosome represented by two kinetochores, which are linked by a spring with stiffness c_k and rest length d_0. Two centrosomes margin the spindle at $\pm x_c$. From each centrosome a constant number M of MTs emerges with their plus ends directed toward the spindle equator. Each MT exhibits dynamic instability [25] and attaches to and detaches from the corresponding kinetochore stochastically. Attached MTs are connected to the kinetochore by a linker, which we model as Hookean polymeric spring with stiffness c and zero rest length. This spring exerts a force $F_{mk} = -c(x_m - X_k)$ on each MT, and each MT exerts a counter force $-F_{mk}$ on the kinetochore, where X_k and x_m are kinetochore and MT position.

In the following we define all MT parameters for MTs in the left half of the spindle model; for MTs in the right half positions, velocities v and forces F have opposite signs. In the left half, tensile forces on the MT–kinetochore link arise for $X_k > x_m$ and pull the MT in the positive x-direction, $F_{mk} > 0$. In [2], the velocities of MT growth v_{m+} and shrinkage v_{m-} as well as the rates of catastrophe ω_c, rescue ω_r and

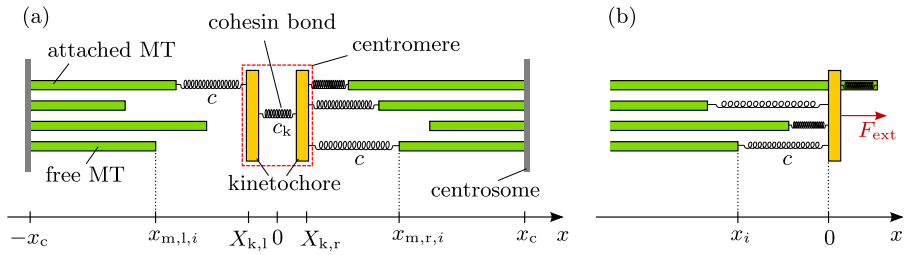

Figure 1. One-dimensional model of the mitotic spindle. (a) Two-sided model: M MT arise from each centrosome and can attach to/detach from the corresponding kinetochore. (b) One-sided model: left half of two-sided model. The cohesin bond is replaced by the external force $F_{\rm ext}$. MTs are not confined by a centrosome and permanently attached to the kinetochore. MT–kinetochore distances $x_i = x_{{\rm m},i} - X_{\rm k}$ are the only relevant coordinates.

Table 2. Model parameters.

Transition parameters	$\omega_{\rm i}$	$\omega_{\rm i}^0$ ($\rm s^{-1}$)	$F_{\rm i}$ (pN)	
Catastrophe	$\omega_{\rm c}$	0.0019	−2.3	[2]
Rescue	$\omega_{\rm r}$	0.024	6.4	[2]
Detachment in growing state	$\omega_{\rm d+}$	0.000 11	3.8	[2]
Detachment in shrinking state	$\omega_{\rm d-}$	0.035	−4.0	[2]
Attachment rate	$\omega_{\rm a}$	1.0	Estimated	
Velocity parameters	$v_{\rm m\pm}$	$v_\pm^0$ ($\rm nms^{-1}$)	$F_\pm$ (pN)	
Growth	$v_{\rm m+}$	5.2	8.7	[2]
Shrinking	$v_{\rm m-}$	−210.0	−3.2	[2]
Other parameters	**Symbol**	**Value**		
Cohesin bond stiffness	$c_{\rm k}$	20 pN $\mu\rm m^{-1}$	Estimated	
Cohesin bond rest length	d_0	1 µm	[7]	
Centrosome position	$x_{\rm c}$	6.8 µm	[10]	
Friction coefficient	γ	1 pN s $\mu\rm m^{-1}$	Estimated	
Thermal energy	$k_{\rm B}T$	4 pN nm	Estimated	

detachment $\omega_{\rm d\pm}$ have been measured while MTs were attached to reconstituted yeast kinetochores. They can all be described by an exponential dependence on the force $F_{\rm mk}$ that acts on the MT plus end:

$$v_{\rm m\pm} = v_\pm^0 \exp\left(\frac{F_{\rm mk}}{F_\pm}\right), \quad \omega_{\rm i} = \omega_{\rm i}^0 \exp\left(\frac{F_{\rm mk}}{F_{\rm i}}\right), \tag{1}$$

(for ${\rm i} = {\rm r}, {\rm c}, {\rm d+}, {\rm d-}$) with $F_+, F_{\rm r}, F_{\rm d+} > 0$ and $F_-, F_{\rm c}, F_{\rm d-} < 0$ for the characteristic forces, because tension ($F_{\rm mk} > 0$) enhances growth velocity, rescue and detachment of a growing MT, while it suppresses shrinking velocity, catastrophe and detachment of a shrinking MT (note that we use signed velocities throughout the paper, i.e., $v_{\rm m-} < 0$ and $v_{\rm m+} > 0$). Suppression of detachment of shrinking MTs is the catch bond property of the MT–kinetochore link. The attachment rate is assumed to follow a Boltzmann distribution,

$$\omega_{\rm a} = \omega_{\rm a}^0 \exp\left(\frac{c(X_{\rm k} - x_{\rm m})^2}{2k_{\rm B}T}\right), \tag{2}$$

according to the MT–kinetochore linker spring energy.

The kinetochore motion is described by an overdamped dynamics,

$$v_{\rm k} \equiv \dot{X}_{\rm k} = \frac{1}{\gamma}\left(F_{\rm kk} + F_{\rm km}\right), \tag{3}$$

with the friction coefficient γ, and the forces $F_{\rm kk}$ and $F_{\rm km} = -\sum_{\rm att.MTs} F_{\rm mk}$ originating from the cohesin bond between kinetochores and the MT–kinetochore linkers of all attached MTs, respectively.

We perform simulations of the model by integrating the deterministic equations of motion for MTs ($\dot{x}_{{\rm m},i} = v_{{\rm m}\pm,i}$ for $i = 1, \ldots, M$) and kinetochores (equation (3)) and include stochastic switching events between growth and shrinking as well as for attachment and detachment to the kinetochore for each MT. For integration we employ an Euler algorithm with a fixed time step $\Delta t \leqslant 10^{-3}$ s which is small enough to ensure $\omega_{\rm i}\Delta t \ll 1$ for all stochastic switching events (see table 2). The algorithm is described in the supplementary material in more detail. We use parameter values from experiments as listed in table 2.

We start with the investigation of the minimal model, i.e. neglecting poleward flux and PEFs and using the same simple spring model for the MT–kinetochore linker as Banigan *et al* where the MT plus ends are able to 'overtake' the kinetochore ($x_m > X_k$, again for MTs in the left half of the spindle) and thereby exert pushing forces $F_{km} > 0$ on the kinetochore (which could be interpreted as a compression of the MT–kinetochore linker). Later, we will generalize the minimal model as described in the introduction, see table 1. In a first step, we add poleward MT flux, which describes a constant flux of tubulin from the plus-ends toward the spindle pole [24], by shifting the MT velocities $v_{m\pm}$. PEFs, which push the kinetochore away from the pole [27], will be included in a second step as external forces, which depend on the absolute positions of the kinetochores. Finally, we will take account of the hypothesis that MTs are not able to apply pushing forces on the kinetochore [7, 26] by modifying the model such that the growth of a MT is stalled or that the MT undergoes a catastrophe when it reaches the kinetochore.

At the centrosome, MTs are confined: It is reasonable to assume that they undergo a forced rescue and detach from the kinetochore if they shrink to zero length. If the mean distance of MTs from the spindle equator is sufficiently small, $|\langle x_m\rangle| \ll |x_c|$, we can also consider the MTs as unconfined ($|x_c| \to \infty$). Then both MT and kinetochore dynamics solely depend on their relative distances and not on absolute positions, which simplifies the analysis.

3. Mean-field theory for bistability in the one-sided model

We first examine the one-sided model of Banigan *et al* [20], which only consists of the left half of the two-sided model with an external force applied to the kinetochore (figure 1(b)). In simulations of this one-sided spindle model, kinetochore movement exhibits bistable behavior as a function of the applied force, i.e., within a certain force range there are two metastable states for the same external force: In one state the MTs predominantly grow and the kinetochore velocity is positive while in the other state the kinetochore has a negative velocity as a consequence of mainly shrinking MTs. It depends on the history which of these two states is assumed: when the system enters the bistable area in consequence of a force change, the kinetochore velocity will maintain its direction (following its current metastable branch) until the force is sufficiently large that the system leaves the bistable area again (the current metastable branch becomes unstable). Later we will show that this hysteresis of the one-sided model can explain stochastic chromosome oscillations in metaphase if two one-sided models are coupled in the full two-sided model.

In the following, we present a Fokker–Planck mean-field approach that lets us derive bistability analytically and obtain constraints for the occurrence of bistability. We obtain a system of Fokker–Planck equations (FPEs) for the M MT–kinetochore distances $x_i \equiv x_{m,i} - X_k$ ($i = 1, \ldots, M$) and decouple the MT dynamics in a mean-field approximation, which neglects kinetochore velocity fluctuations.

We make two assumptions. First we assume that all M MTs are always attached to the kinetochore. Because the MT–kinetochore links are catch bonds this assumption is equivalent to assuming that these links are predominantly under tension. We will check below by comparison with numerical simulations to what extent this assumption can be justified. Secondly, we neglect that MTs are confined by a centrosome. Then, as mentioned above, the only relevant coordinates are the relative MT–kinetochore distances x_i, which measure the extension of the ith linker.

The MTs are coupled because they attach to the same kinetochore: each MT experiences a force $F_{mk,i} = -cx_i$ from the elastic linker to the kinetochore, which is under tension (compression) for $x_i < 0$ ($x_i > 0$); the kinetochore is subject to the total counter force $F_{km} = c\sum_i x_i$. Therefore, the kinetochore velocity v_k is a stochastic variable depending on *all* distances x_i, on the one hand, but determines the velocities $\dot{x}_i = v_{m\pm}(x_i) - v_k$ of MTs relative to the kinetochores, on the other hand. The equations can be decoupled to a good approximation because the one-sided system assumes a steady state with an approximately stationary kinetochore velocity v_k after a short time (rather than, for example, a cooperative oscillation as for an MT ensemble pushing against an elastic barrier [38]). In our mean-field approximation we then assume a constant kinetochore velocity $v_k \equiv \langle v_k\rangle$ and neglect all stochastic fluctuations around this mean. This mean value is determined by the mean linker extension $\langle x\rangle$ via

$$v_k = \frac{1}{\gamma}\left(F_{ext} + cM\langle x\rangle\right). \tag{4}$$

Fluctuations around the mean value are caused by fluctuations of the force $F_{km} = c\sum_i x_i$ around its mean $\langle F_{km}\rangle = Mc\langle x\rangle$, which become small for large M (following the central limit theorem).

If v_k is no longer a stochastic variable, the dynamics of the MT–kinetochore extensions x_i decouple. Then, the probability distribution for the M extensions x_i factorizes into M identical factors $p_\pm(x_i, t)$, where

Table 3. Maximal or a minimal value $x_{\max}$ or $x_{\min}$ of the stationary linker extension distribution $p(x)$ from conditions $v_-(x_{\min}) = 0$ and $v_+(x_{\max}) = 0$. The distance $x_{\min}$ ($x_{\max}$) is a function of the prescribed kinetochore velocity v_k and has to be specified separately depending on the direction of v_k; $x_{\min}$ ($x_{\max}$) is approached if the MTs shrink (grow) for a sufficiently long time.

	MT shrinks	MT grows
$v_k > 0$	$v_-(x) < -v_k$ always $x_{\min} = -\infty$	$v_+(x) > 0$ for $x < x_{\max}$ $x_{\max} = (F_+/c) \ln\left(v_+^0/v_k\right)$
$v_k < 0$	$v_-(x) < 0$ for $x > x_{\min}$ $x_{\min} = (F_-/c) \ln\left(v_-^0/v_k\right)$	$v_+(x) > v_k$ always $x_{\max} = \infty$
$v_k = 0$	$v_-(x) < 0$ always $x_{\min} = -\infty$	$v_+(x) > 0$ always $x_{\max} = \infty$

$p_\pm(x,t)$ are the probabilities to find one particular MT in the growing ($+$) or shrinking ($-$) state with an MT–kinetochore linker extensions x. We can derive two FPEs for the dynamical evolution of $p_\pm(x,t)$,

$$\partial_t p_+(x,t) = -\omega_c(x) p_+(x,t) + \omega_r(x) p_-(x,t) - \partial_x \left(v_+(x) p_+(x,t)\right), \tag{5}$$

$$\partial_t p_-(x,t) = \omega_c(x) p_+(x,t) - \omega_r(x) p_-(x,t) - \partial_x \left(v_-(x) p_-(x,t)\right), \tag{6}$$

where $v_\pm(x)$ denotes the relative velocity of MT and kinetochore,

$$v_\pm(x) \equiv v_{m\pm}(x) - v_k = v_\pm^0 \exp\left(-\frac{cx}{F_\pm}\right) - v_k, \tag{7}$$

and $\omega_{c,r}(x) = \omega_{c,r}^0 \exp\left(-cx/F_{c,r}\right)$. The velocity v_k is no longer stochastic but self-consistently determined by (4). We note that these FPEs are equivalent to single MT FPEs with position-dependent velocities, catastrophe and rescue rates [39–42].

We will now obtain the force–velocity relation of the whole MT ensemble by first solving the FPEs (5) and (6) in the stationary state $\partial_t p_\pm(x,t) = 0$ and then calculating the mean linker extension $\langle x \rangle$ for given kinetochore velocity v_k using the stationary distribution $p_\pm(x)$. The external force that is necessary to move the kinetochore with velocity v_k then follows from (4),

$$F_{ext} = \gamma v_k - cM\langle x \rangle(v_k). \tag{8}$$

The MT–kinetochore distance x is limited to a maximal or a minimal value $x_{\max}$ or $x_{\min}$ for a given kinetochore velocity $v_k > 0$ or < 0, respectively, see table 3. These limiting values are reached if the relative MT–kinetochore velocities vanish after the linker extension x has adjusted: first we consider $v_k < 0$ and a shrinking MT. If we start with a compressed linker ($x > 0$), the MT starts to shrink fast, the compression is reduced and the linker may get under tension ($x < 0$) because the relative velocity is negative, $\dot{x} = v_-(x) < 0$. The MT–kinetochore distance x continues to decrease until $\dot{x} = v_-(x_{\min}) = 0$ in (7), where the shrinking velocity of the MTs is the same as the prescribed kinetochore velocity ($v_{m-} = v_k$). Further shrinking to $x < x_{\min}$ is not possible but distances $x > x_{\min}$ can always be reached if MTs are rescued. If $v_k < 0$ and the MT grows, on the other hand, there is no upper bound on x, as the relative velocity $\dot{x} = v_+(x)$ is always positive; x starts to grow into the compressive regime $x > 0$ and continues to grow without upper bound (for very large compressive linker extensions, MT growth is suppressed, but the kinetochore still moves such that $v_+(x) \approx -v_k > 0$). Analogously, if $v_k > 0$ and MTs grow, x grows until $\dot{x} = v_+(x_{\max}) = 0$, and smaller distances can be reached by catastrophe but there is no lower bound on x for shrinking MTs. Linker extensions $x_{\max}$ ($x_{\min}$) are reached as stationary states if catastrophes (rescues) are suppressed (for example, because of large forces), such that MTs can grow (shrink) for sufficiently long times. If the external force F_{ext} is prescribed rather than a kinetochore velocity, all MTs reach a stationary state with the same velocity $\tilde{v}_\pm$ given by (8), $F_{ext} = \gamma\tilde{v}_\pm - cMx_{\max,\min}$. In this stationary state, both MT-tips and kinetochore move with the same velocity

$$\tilde{v}_\pm \equiv \frac{MF_\pm}{\gamma} W\left(\frac{\gamma v_\pm^0}{MF_\pm} \exp\left(\frac{F_{ext}}{MF_\pm}\right)\right), \tag{9}$$

where $W()$ denotes the Lambert-W function (defined by $x = W(x)e^{W(x)}$).

In the complete absence of stochastic switching between growth and shrinking by catastrophes and rescues, the MT ensemble reaches stationary states with peaked distributions $p_+(x) \propto \delta(x_{\max} - x)$ and $p_-(x) \propto \delta(x - x_{\min})$. Stochastic switching shifts and broadens these peaks, and the FPEs (5) and (6) lead to a distribution $p_\pm(x,t)$ of linker extensions x in the growing and shrinking states with statistical weight

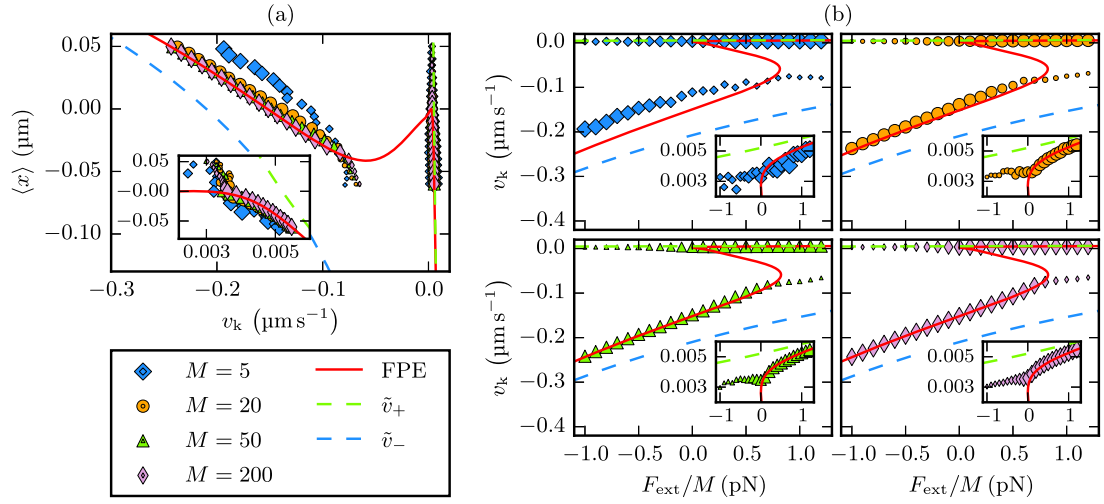

Figure 2. Mean-field results compared to stochastic simulations of the one-sided model. (a) The master curve $\langle x \rangle(v_k)$ from the mean-field approach (red line) agrees with simulation results for different MT-numbers $M = 5, 20, 50, 200$. The dashed lines mark $x_{min,max}(v_k)$ from table 3. We run simulations with constant external forces and average over 80 simulations for each force. Initially, the MT–kinetochore distance is either x_{min} or x_{max} while all MTs grow or shrink with velocity $\tilde{v}_\pm$, respectively. The system then enters a (meta-)stable state, in which we measure the mean kinetochore velocity and MT–kinetochore distances. The marker size depicts the time the system rests in this state on average, which is a measure for its stability (maximum marker size corresponds to $t_{rest} \geqslant 1000$ s). As predicted, the mean-field approach turns out to be correct in the limit of many MTs, and in this limit the $\langle x \rangle(v_k)$-relation is independent of the MT-number M. (b) Resulting force–velocity relations for different MT-numbers $M = 5, 20, 50, 200$. The dashed lines show the large velocity limit $v_k \approx \tilde{v}_\pm$ given by (9). We used a linker stiffness of $c = 20$ pN μm^{-1} both in (a) and (b).

$p_\pm(x,t) > 0$ in the whole interval $x_{min} \leqslant x \leqslant x_{max}$. At the boundaries x_{min} and x_{max} of this interval, the probability current density

$$j(x,t) \equiv v_+(x,t)p_+(x,t) + v_-(x,t)p_-(x,t) \tag{10}$$

has to vanish. Furthermore, in any stationary state ($\partial_t p_\pm(x,t) = 0$) the current density is homogeneous, as can be seen by summing up the FPEs (5) and (6):

$$0 = \partial_x(v_+(x)p_+(x) + v_-(x)p_-(x)) = \partial_x j(x). \tag{11}$$

Together with $j = 0$ at the boundaries this implies that $j = 0$ everywhere in a steady state. The resulting relation $v_+(x)p_+(x) = -v_-(x)p_-(x)$ can be used to reduce the stationary FPEs to a single ordinary differential equation with the solution [41]

$$p_\pm(x) = \frac{\pm\mathcal{N}}{v_\pm(x)} \exp\left(-\int\left(\frac{\omega_c(x)}{v_+(x)} + \frac{\omega_r(x)}{v_-(x)}\right)\mathrm{d}x\right) \tag{12}$$

for the stationary distribution of linker extensions x in the growing and shrinking states. The normalization constant $\mathcal{N}$ must be chosen so that the overall probability density $p(x) \equiv p_+(x) + p_-(x)$ satisfies $\int_{x_{min}}^{x_{max}} p(x)\mathrm{d}x = 1$. Obviously, $p_\pm(x) = 0$ for $x > x_{max}$ and $x < x_{min}$. The stationary probability densities $p_\pm(x)$ from (12) can then be used to calculate the mean distance $\langle x \rangle$ as a function of the kinetochore velocity v_k, which enters through (7) for $v_\pm(x)$. The integral in the exponent in (12) as well as the normalization can be evaluated numerically to obtain an explicit $\langle x \rangle(v_k)$-relation, which is shown in figure 2(a).

At this point it should be noticed that in the mean-field theory the $\langle x \rangle(v_k)$-relation is *independent* of the MT number M. Therefore, we call it *master curve* henceforth. In figure 2(a) we compare the mean-field theory result to stochastic simulations and find that the mean-field approach becomes exact in the limit of large M, where fluctuations in the kinetochore velocity around its mean in (4) can be neglected.

The master curve is a central result and will be the basis for all further discussion. Together with the force-balance (8) on the kinetochore, the master curve will give the force–velocity relation for the MT–kinetochore system. A positive slope of the master curve, as it can occur for small $v_k \approx 0$ (see figure 2(a)), gives rise to an instability of the MT–kinetochore system: then, a positive kinetochore velocity fluctuation $\delta v_k > 0$ leads to an MT–kinetochore linker compression $\delta\langle x \rangle > 0$. According to the

force-balance (8), a compression $\delta\langle x\rangle > 0$ puts additional forward-force on the kinetochore leading to a positive feedback and further increase $\delta v_\mathrm{k} > 0$ of the kinetochore velocity. This results in an instability, which will prevent the system to assume mean linker extensions $\langle x\rangle$ in this unstable regime. This is confirmed by stochastic simulation results in figure 2(a), which show that the unstable states are only assumed transiently for very short times. Therefore, occurrence of a positive slope in the master curve in figure 2(a) is the essential feature that will give rise to bistability in the one-sided model and, finally, to oscillations in the full two-sided model.

Now we want to trace the origin of this instability for small $v_\mathrm{k} \approx 0$. If the MTs are growing (shrinking) for a long time, all linker extensions assume the stationary values $x \approx x_\mathrm{max}(v_\mathrm{k})$ ($x \approx x_\mathrm{min}(v_\mathrm{k})$) from table 3, where the MT-velocity adjusts to the kinetochore velocity, $v_\mathrm{k} \approx v_{\mathrm{m}\pm}(x)$. If the kinetochore velocity increases in these states by a fluctuation (i.e., $\delta v_\mathrm{k} > 0$), the MT–kinetochore linkers are stretched (i.e., $\delta x < 0$), which slows the kinetochore down again resulting in a stable response. This is reflected in the negative slopes of both $x_\mathrm{max}(v_\mathrm{k})$ (for $v_\mathrm{k} > 0$) and $x_\mathrm{min}(v_\mathrm{k})$ (for $v_\mathrm{k} < 0$). Because of constant stochastic switching between catastrophes and rescues the mean linker extension exhibits fluctuations about x_max and x_min, but we expect also the master curve $\langle x\rangle(v_\mathrm{k})$ to have a negative slope for a wide range of velocities v_k. Figure 2(a) shows that this is actually the case for kinetochore velocities v_k around the force-free growth or shrinking velocities $v_\pm^0$ of the MTs, i.e., if the imposed kinetochore velocity v_k roughly 'matches' the force-free growing or shrinking MT velocity. Then a small mismatch can be accommodated by small linker extensions x, which do not dramatically increase fluctuations by triggering catastrophe or rescue events.

The situation changes for small negative or small positive values of the kinetochore velocity around $v_\mathrm{k} \approx 0$. For $v_\mathrm{k} \lesssim 0$, MT–kinetochore linkers develop logarithmically growing large negative extensions x_min (see table 3) corresponding to a slow kinetochore trailing fast shrinking MTs that strongly stretch the linker. Likewise, for $v_\mathrm{k} \gtrsim 0$, MT–kinetochore linkers develop logarithmically growing large positive extensions x_max corresponding to a slow kinetochore trailing fast growing MTs that strongly compress the linker. Around $v_\mathrm{k} \approx 0$, the system has to switch from large negative x to large positive x because the resulting tensile force $F_\mathrm{mk} = -cx$ on the shrinking MT will destabilize the shrinking state and give rise to MT rescue at least for $x < -F_\mathrm{r}/c$.

Therefore, also the mean value $\langle x\rangle$ switches from negative to positive values resulting in a positive slope of the master curve if the stationary distributions $p_-(x)$ and $p_+(x)$ remain sufficiently peaked around the linker extensions x_min and x_max, also in the presence of fluctuations by catastrophes and rescues. In the supplementary material, we show that the stationary distributions assume a power-law behavior $p_+(x) \propto (x_\mathrm{max} - x)^{\alpha_+}$ [$p_-(x) \propto (x - x_\mathrm{min})^{\alpha_-}$] around x_max [x_min] for $v_\mathrm{k} > 0$ [$v_\mathrm{k} < 0$] with exponents $\alpha_\pm$ that depend on the MT–kinetochore stiffness c as $\alpha_\pm + 1 \propto 1/c$ in the presence of fluctuations. It follows that distributions are peaked (i.e., have a large kurtosis) and bistability emerges if the MT–kinetochore linker stiffness c is sufficiently large such that deviations of the MT velocity from the kinetochore velocity become suppressed by strong spring forces. This is one of our main results. We also find that $\alpha_\pm + 1 \propto (|v_\mathrm{k}/v_\pm^0|)^{-1-|F_\pm/F_\mathrm{c,r}|}$ such that the distributions become also peaked around $x_\mathrm{min,max}$ in the limit of large velocities $|v_\mathrm{k}|$. Then the velocity approaches $v_\mathrm{k} \approx \tilde{v}_\pm(F_\mathrm{ext})$ for a prescribed external force such that $\tilde{v}_\pm$ from (9) represents the large velocity and large force limit of the force–velocity relation of the kinetochore (see figure 2(b)).

In the unstable regime around $v_\mathrm{k} \approx 0$, the linker length distribution $p(x)$ is typically broad without pronounced peaks and has a minimal kurtosis (as a function of v_k) in the presence of catastrophe and rescue fluctuations. In this regime the system assumes a state with a heterogeneous stationary distribution of growing and shrinking MTs, i.e., the total probabilities to grow or shrink become comparable, $\int p_+(x)\mathrm{d}x \sim \int p_-(x)\mathrm{d}x$. If the kinetochore velocity is increased, $\delta v_\mathrm{k} > 0$, the system does not react by $\delta x < 0$, i.e., by increasing the average tension in the linkers in order to pull MTs forward, but by *switching* MTs from the shrinking to the growing state (on average), which then even allows to relax the average linker tension.

Using the force-balance (8) on the kinetochore, the master curve is converted to a force–velocity relation for the MT–kinetochore system; the results are shown in figure 2(b). The bistability in the master curve directly translates to a bistability in the force–velocity relation of the MT ensemble, and we obtain a regime with three branches of possible velocities for the same external force. The upper and the lower branches agree with our simulation results and previous simulation results in [20], and our mean-field results become exact in the limit of large M, see figure 2(b). These branches correspond to the two stable parts of the master curve with negative slope, that are found for kinetochore velocities v_k roughly matching the force-free growth or shrinking velocities $v_\pm^0$ of the MTs. The mid branch corresponds to the part of the master curve with positive slope, where the system is unstable. Also figure 2(b) demonstrates that this instability is confirmed by stochastic simulations results.

Finally, we note that a simpler theoretical approach, where it is assumed that all linkers assume *identical* extensions $x_i \approx x$ and all attached MTs are in the same state (growing or shrinking), is exact for a single MT ($M = 1$) by definition but not sufficient to obtain a bistable force–velocity relation for MT ensembles ($M > 1$) (see supplementary material). The same assumption of identical MT positions has already been used to study an ensemble of MTs that are connected to the same kinetochore via Hill sleeve like linkers [17, 29]. The model of Klemm *et al* [21] divides each MT ensemble into a growing and a shrinking sub-ensemble, and assumes equal load sharing only between MTs within each sub-ensemble. We can show that, together with a force-sensitive rescue force, this is sufficient to obtain a bistable force–velocity relation in a corresponding one-sided model.

4. Bistability gives rise to oscillations in the two-sided model

As already worked out by Banigan *et al* [20], the bistability in the force–velocity relation of the one-sided MT ensemble can be considered to be the cause for stochastic oscillations in the two-sided model. Each ensemble can be either on the lower branch of the force–velocity relation, where it mainly depolymerizes and exerts a P-directed pulling force ($v_\mathrm{k} < 0$) or on the upper branch where it mainly polymerizes and exerts an AP-directed pushing force ($v_\mathrm{k} > 0$). The external force in the one-sided model is a substitute for the spring force $F_\mathrm{kk} = c_\mathrm{k}\left(X_\mathrm{k,r} - X_\mathrm{k,l} - d_0\right)$ of the cohesin bond in the full model with a stiffness c_k and rest length d_0, see table 2. Since the cohesin force is a linear function of the inter-kinetochore distance, the force–velocity relation can be treated as distance-velocity (phase space) diagram for the two kinetochores (see figure 3(a)), where both kinetochores move as points on the force–velocity relation. The cohesin bond always affects the two kinetochores in the same way because action equals reaction: if the cohesin spring is stretched, both kinetochores are pulled away from their pole (AP), if it is compressed, both kinetochores are pushed polewards (P). Thus, the kinetochores always have the same position on the F_kk-axis in the F_kk–v_k-diagram in figure 3(a), if F_kk on the horizontal axis is defined as the force on the kinetochore in AP-direction (i.e., $F_\mathrm{kk,l} \equiv F_\mathrm{kk}$ and $F_\mathrm{kk,r} \equiv -F_\mathrm{kk}$ for the left/right kinetochore). Likewise, we define v_k on the vertical axis as the velocity in AP-direction (i.e., $v_\mathrm{k,l} \equiv \dot{X}_\mathrm{k,l}$ and $v_\mathrm{k,r} \equiv -\dot{X}_\mathrm{k,r}$ for the left/right kinetochore). The upper/lower stable branch of the force–velocity relation is denoted by $v_\mathrm{k}^{\pm}(F_\mathrm{kk})$. Typically, a kinetochore on the upper (lower) branch has $v_\mathrm{k}^{+} > 0$ ($v_\mathrm{k}^{-} < 0$) and, thus moves in AP-(P-)direction. Using $F_\mathrm{kk} = c_\mathrm{k}\left(X_\mathrm{k,r} - X_\mathrm{k,l} - d_0\right)$ for the spring force, we find $\dot{F}_\mathrm{kk} = -c_\mathrm{k}\left(v_\mathrm{k,r} + v_\mathrm{k,l}\right)$, i.e., kinetochores move with the sum of their AP-velocities along the force–velocity curve in the F_kk–v_k diagram.

Oscillations arise from the two kinetochores moving through the hysteresis loop of the bistable force–velocity relation as described in figure 3(a). Three states are possible (see figure 3(b)). In state 0, both kinetochores move in AP-direction (i.e., in opposite directions) relaxing the F_kk-force from the cohesin bond, i.e., on the upper branch and to the left in the v_k–F_kk-diagram with velocity $\dot{F}_\mathrm{kk} = -2c_\mathrm{k}v_\mathrm{k}^{+} < 0$. After reaching the lower critical force F_min of the hysteresis loop, one of the two kinetochores reverses its direction and switches to the lower branch resulting into states 2 or 2′ where one kinetochore continues in AP-direction with $v_\mathrm{k}^{+} > 0$ while the other is moving in P-direction with $v_\mathrm{k}^{-} < 0$ (i.e., both move in the same direction). In the v_k–F_kk-diagram, this results in a motion to the right with velocity $\dot{F}_\mathrm{kk} = c_\mathrm{k}(-v_\mathrm{k}^{-} - v_\mathrm{k}^{+}) > 0$ because MTs typically shrink much faster than they grow ($-v_{-}^{0} \gg v_{+}^{0}$, see table 2). Moving on opposite P- and AP-branches increases the kinetochore distance and builds up F_kk-force in the cohesin bond. After reaching the upper critical force F_max of the hysteresis loop, it is always the kinetochore on the lower branch moving in P-direction which switches back and state 0 is reached again. This behavior is in agreement with experimental results [11]. The system oscillates by alternating between state 0 and one of the states 2 or 2′ (which is selected randomly with equal probability).

For each of the states 0, 2 and 2′ depicted in figures 3(a) and (b) the two branches $v_\mathrm{k}^{\pm} = v_\mathrm{k}^{\pm}[F_\mathrm{kk}]$ provide deterministic equations of motion for the kinetochore positions. Inserting $F_\mathrm{kk} = c_\mathrm{k}\left(X_\mathrm{k,r} - X_\mathrm{k,l} - d_0\right)$ we obtain both kinetochore velocities as functions of the kinetochore positions and find

$$\begin{aligned}
\text{state 0:}\quad & \dot{X}_\mathrm{k,l} = v_\mathrm{k}^{+}\left[c_\mathrm{k}\left(X_\mathrm{k,r} - X_\mathrm{k,l} - d_0\right)\right] > 0,\\
& \dot{X}_\mathrm{k,r} = -v_\mathrm{k}^{+}\left[c_\mathrm{k}\left(X_\mathrm{k,r} - X_\mathrm{k,l} - d_0\right)\right] < 0,\\
\text{state 2:}\quad & \dot{X}_\mathrm{k,l} = v_\mathrm{k}^{-}\left[c_\mathrm{k}\left(X_\mathrm{k,r} - X_\mathrm{k,l} - d_0\right)\right] < 0,\\
& \dot{X}_\mathrm{k,r} = -v_\mathrm{k}^{+}\left[c_\mathrm{k}\left(X_\mathrm{k,r} - X_\mathrm{k,l} - d_0\right)\right] < 0,\\
\text{state 2}'\text{:}\quad & \dot{X}_\mathrm{k,l} = v_\mathrm{k}^{+}\left[c_\mathrm{k}\left(X_\mathrm{k,r} - X_\mathrm{k,l} - d_0\right)\right] > 0,\\
& \dot{X}_\mathrm{k,r} = -v_\mathrm{k}^{-}\left[c_\mathrm{k}\left(X_\mathrm{k,r} - X_\mathrm{k,l} - d_0\right)\right] > 0.
\end{aligned} \tag{13}$$

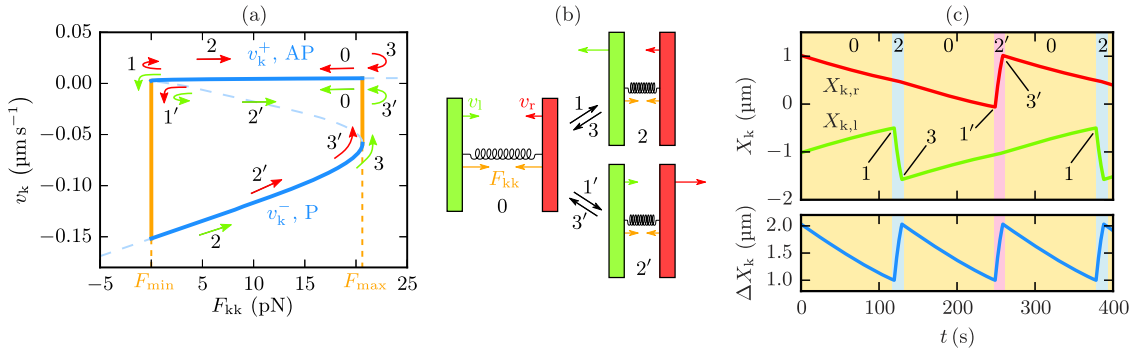

Figure 3. Bistability gives rise to oscillations in the two-sided model. (a) and (b) Different states of sister kinetochore motion can be deduced from the bistability of the force–velocity relation: either both kinetochores are in the upper branch (0) or one is in the upper and the other one in the lower branch (2, 2′). In the first case, both kinetochores move away from their pole (AP) toward each other. Thus, the spring force F_{kk} decreases until it reaches F_{min}. Since the upper branch is not stable anymore below F_{min}, either the left (1) or the right (1′) kinetochore switches to the lower branch and changes direction to poleward movement (P). The system is then in state 2 or 2′, where both kinetochores move into the same direction: the leading kinetochore P, the trailing kinetochore AP. As P—is much faster than AP-movement (MT shrinking is much faster than growth), the inter-kinetochore distance and the spring force are increasing. Above F_{max} only AP-movement is stable, which is why the leading kinetochore changes direction (3, 3′) and the system switches to state 0 again. (c) Solution of the equations of motion (13) for $c = 20$ pN μm^{-1} and $M = 25$ with an imposed periodic order of states (0–2–0–2′–0– . . .). The initial condition is $F_{kk} = F_{max}$ (both kinetochores at the right end of the upper branch). For an animated version see video S1 in the supplementary material.

Solving these equations gives idealized deterministic trajectories of the sister kinetochores, when we also assume that the left and the right kinetochore pass the lower branch alternately such that the order of states is a periodic sequence 0–2–0–2′–0– . . . as shown in the example in figure 3(c). Then single kinetochores oscillate with half the frequency of inter-kinetochore (breathing) oscillations, just as observed in PtK1 cells [11]. Moreover, we can obtain numerical values of the frequencies directly from the trajectories. For an MT–kinetochore linker stiffness $c = 20$ pN μm^{-1} and 20–25 MTs per kinetochore, which is a realistic number for mammalian cells [43], we get periods of 206–258 s and 103–129 s for kinetochore and breathing oscillations, respectively. These values coincide with experimental results of 239 s and 121 s measured in PtK1 cells [11].

The calculated trajectories are idealized since they neglect stochastic fluctuations that occur in simulations of the two-sided model and have two main effects on the kinetochore dynamics which already arise in simulations that comply with the assumptions behind the mean-field theory (no confinement ($x_c \to \infty$) and permanent bonds ($\omega_d = 0$)): firstly, the sister kinetochores do not pass the lower branch alternately but in random order. Therefore, we observe phases where one kinetochore moves in AP-direction for several periods, while the other one changes its direction periodically but moves polewards on average (figure 4(a)). Since this does not influence the trajectory of the inter-kinetochore distance, breathing oscillations still occur in a more or less regular manner, which allows us to measure their frequencies by Fourier analysis. We will show below that additional polar ejection forces suppress this random behavior and force the kinetochores to pass the lower branch alternately. As a second effect of the stochastic character of the simulation, kinetochores do not change the branch instantaneously after crossing the critical forces F_{max} or F_{min}. Instead, they tend to maintain their primary state for a while (figure 4(b)) and follow the metastable states that we also observe in the one-sided model (figure 2(b)). Hence, the frequencies we measure in the simulations are smaller than those we calculate from the Fokker-Planck mean-field approach (figure 4(c)). The latter effect vanishes in the limit of many MTs (large M): the switching points approach the theoretical values F_{max} and F_{min}, and the simulated breathing frequencies converge to our mean-field predictions.

So far we have demonstrated that the mean field theory correctly describes kinetochore dynamics in simulations of the unconfined model where we suppress detachment in order to prevent unattached MTs from shrinking toward infinity. As shown in figure 5(a) and (b), kinetochore oscillations also survive in simulations of the confined model independently of whether the MTs are able to detach from the kinetochore, i.e., to rupture the catch bond. However, confinement by the centrosome influences the kinetochore dynamics in the limit of large M: since more MTs exert a higher force on the kinetochore, it is possible that one of the two sisters gets stuck at the centrosome for a while (see figure 5(a) and (b)). Hence, the frequencies measured in the confined two-sided model deviate from the frequencies in the unconfined case above $M \approx 200$.

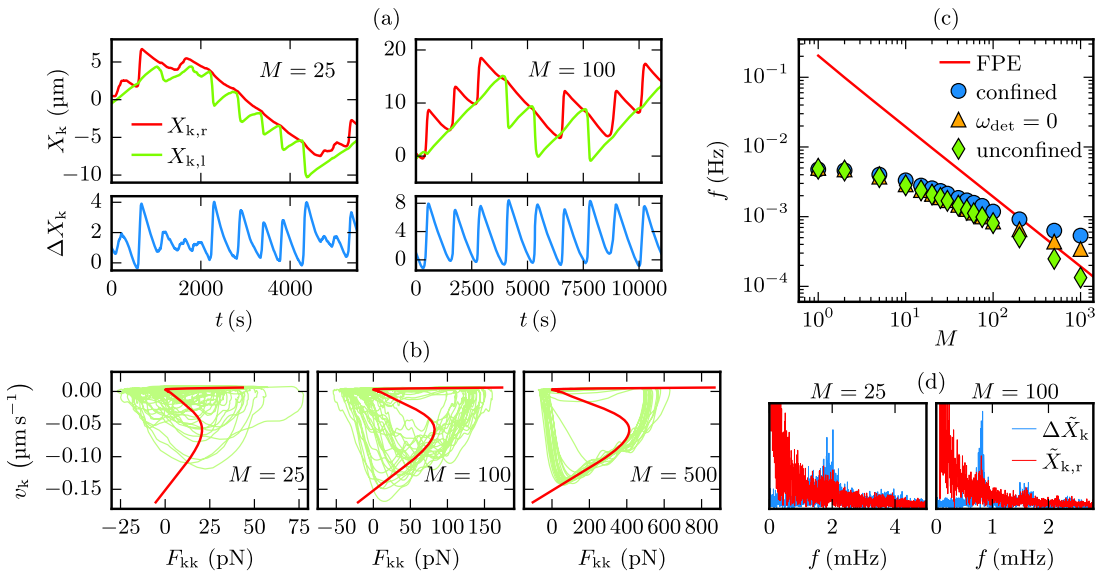

Figure 4. Oscillations in stochastic simulations of the unconfined model compared to mean-field results. (a) Kinetochore trajectories and breathing oscillations in the two-sided model without confinement ($x_c \to \infty$) and detachment ($\omega_d = 0$). The kinetochores behave as described in figure 3 with a random order of states $2/2'$. The breathing oscillations are regular enough to assign a frequency by Fourier analysis, see (d). With less MTs oscillations are more fluctuative. (b) Kinetochore velocity against cohesin force in simulations of the unconfined two-sided model without detachment (green). For many MTs the velocity follows very precisely the predicted hysteresis from the mean-field approach (red). For animated versions see videos S2 ($M = 25$) and S3 ($M = 500$) in the supplementary material. (c) Double-logarithmic plot of frequencies of breathing oscillations as a function of MT number M: calculated from the mean-field approach according to figure 3 (red) and measured in simulations of the unconfined (green diamonds) as well as the confined model with detachable catch bonds (blue circles) and with permanent attachment (orange triangles). Confinement becomes relevant for large MT numbers. In the presence of detachable catch bonds only 75% of the MTs are attached on average, which corresponds to a simple shift of the curve to lower MT numbers. (d) Trajectories from (a) in Fourier space. While $\tilde{X}_{k,r}$ has its maximum at $f = 0$ due to the random order of states in figure 3, $\Delta\tilde{X}_k$ has a distinct peak that becomes sharper for large M indicating regular breathing oscillations. For all simulations the MT–kinetochore linker stiffness was $c = 20$ pN μm^{-1}.

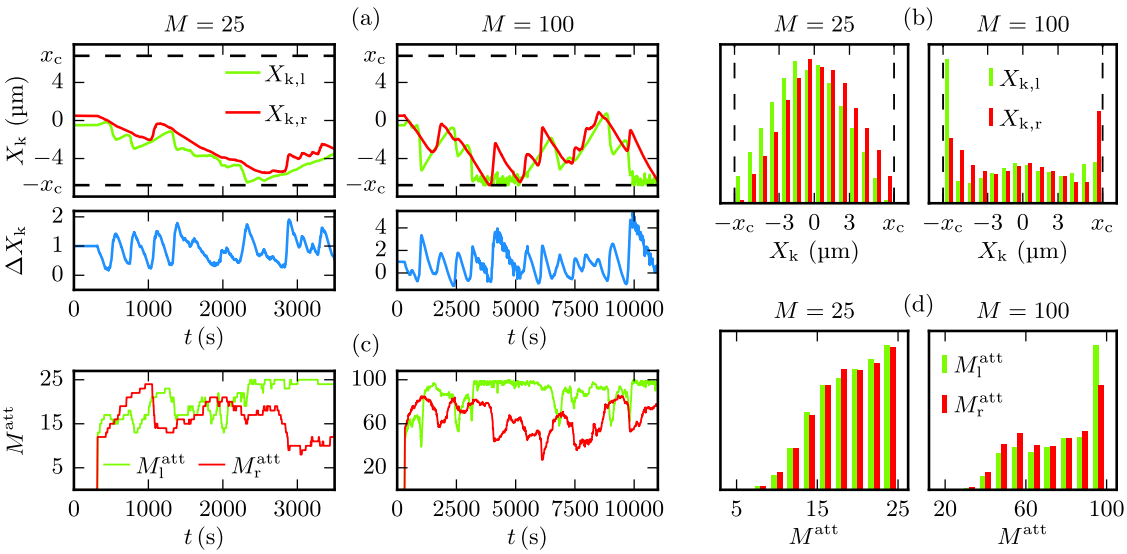

Figure 5. Dynamics in the confined model with detachable MTs. (a) Kinetochore positions X_k and inter-kinetochore distance ΔX_k over time in simulations with a total number of $M = 25$ and $M = 100$ MTs per spindle pole. Oscillations as described in figure 3 are recognizable. With 100 MTs one kinetochore can get stuck to the centrosome for a while. (b) Distribution of kinetochore positions. The kinetochores are not aligned to the spindle equator and for $M = 100$ they are most likely to be found near the centrosomes. (c) Number of attached MTs M^{att} over time. MTs are more likely to be attached when the correspondent kinetochore is near the centrosome since the free MTs can reattach to the kinetochore faster in that case. (d) Distribution of M^{att}. On average 75% of the MTs are attached independently of the total MT number M.

If we enable detachment in our simulations we find that the number of attached MTs correlates with the kinetochore position (see figure 5(c)) since due to the exponential distribution of free MTs and the distance dependent attachment rate (2) detached MTs are more likely to reattach to the kinetochore the closer it is to the centrosome. Moreover, on average, about 75% of the MTs are attached independently of the total MT number (see figures 5(c) and (d)). Therefore, the catch bond nature of the link leads to an effective behavior similar to a system without detachment but with less MTs, which explains the difference in frequencies between the confined models with and without detachment in figure 4(c). We conclude that detachment does not play a major role for the occurrence of kinetochore oscillations in cells with many MTs as despite detachment there are always enough MTs attached to justify our mean-field approximation. Hence, (periodic) changes in the number of attached MTs as they can be seen in figure 5(c) are rather a passive consequence than an active source of kinetochore oscillations. This argumentation may not be tenable, if just a few MTs are attached to a kinetochore, so that even detachment of a single MT effects the total force acting on the kinetochore significantly. Then, detachment can be the primary cause of directional instability as worked out by Gay *et al* [44], who modeled the mitotic spindle of fission yeast.

Taking into account the results of the last paragraph, we will mainly investigate the unconfined model with permanently attached MTs in the following sections. This procedure is reasonable as we do not lose any qualitative key features of kinetochore dynamics on the one hand, and, on the other hand, gain a much better comparability of our mean field theory with the appropriate stochastic simulations.

We finally note that in all cases we examined (confined/unconfined system, permanent/detachable bonds) the kinetochore oscillations become more fluctuative if less MTs are attached. This leads to the conclusion that kinetochore oscillations are a result of the collective dynamics of an ensemble of MTs that exhibit a force-dependent dynamic instability individually. Such a behavior cannot be described correctly based on the simple assumption that all linkers have the same extension, i.e., that MTs share the load equally and all attached MTs are in the same state (growing or shrinking), (see supplementary material). Therefore, the model of Shtylla and Keener [17] which does assume equal load sharing and synchronous MT dynamics requires a chemical feedback as an additional mechanism in order to obtain kinetochore oscillations. The model of Klemm *et al* [21] divides each MT ensemble into a growing and a shrinking sub-ensemble, and assumes equal load sharing only between MTs within each sub-ensemble. Together with a force-sensitive rescue force, this is sufficient to obtain oscillations.

5. Constraints on linker stiffness and MT number for bistability and oscillations

5.1. Constraints for bistability in the one-sided model

We already argued above in section 3 that bistability (and thus oscillations) can only emerge if the MT–kinetochore linker is sufficiently stiff. To analyze the influence of the linker stiffness c and the MT number M on bistability quantitatively, the transformation from the master curve to the force–velocity relation is visualized in figure 6(a) as search for the intersections of the master curve with linear functions

$$\langle x\rangle = \frac{1}{cM}(\gamma v_{\mathrm{k}} - F_{\mathrm{ext}}). \tag{14}$$

In the limit of large M these linear functions have zero slope. Bistable force–velocity relations with three intersection points are only possible if the master curve has positive slope for intermediate v_{k} resulting in a maximum and minimum. The extrema of the master curve vanish, however, in a saddle-node bifurcation if the linker stiffness drops below $c_{\mathrm{bist}} = 7.737$ pN μm^{-1}, which is, therefore, a lower bound for the occurrence of bistability. In the case of finite MT numbers M, bistable force–velocity relations can only be found if the slope in the inflection point of the master curve exceeds γ/cM (the slope of the linear function (14)). This allows us to quantify a bistable regime in the parameter plane of linker stiffness c and MT number M as shown in figure 6(b).

5.2. Constraints for oscillations in the two-sided model

We showed in section 4 that bistability of the one-sided model is a necessary condition for oscillations in the two-sided model. Now we show that bistability in the one-sided model is, however, *not sufficient* for oscillations in the full model. If the force–velocity relation is interpreted as phase space diagram for the two kinetochores, kinetochores only switch branches in the v_{k}–F_{kk}-diagram if their velocity changes its sign at the turning points F_{min} and F_{max}. If this is not the case and one of the two branches crosses $v_{\mathrm{k}} = 0$ (e.g. the right branch for $c = 10$ pN μm^{-1} in figure 6(a), which transforms to the upper branch of the force–velocity relation), the intersection point is a stable fixed point in the phase space diagram (see figure 7(a)). At this

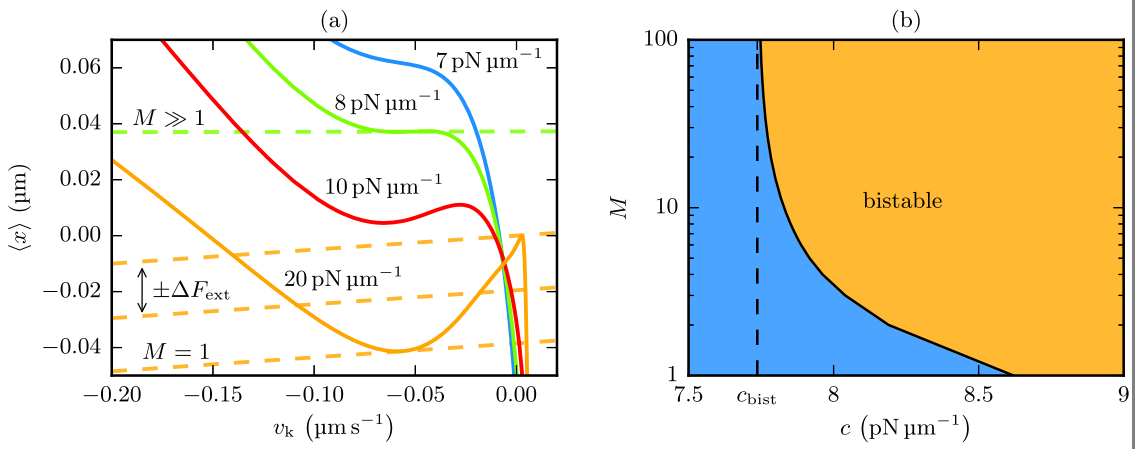

Figure 6. Constraints for bistability in the one-sided model. (a) Master curves for different linker stiffnesses c and linear functions according to (14). In the limit of large M the linear functions have zero slope and bistability occurs if the master curve has two extrema, which is the case for $c > c_{\rm bist}$. For finite M bistable solutions are possible if the linear functions have a smaller slope than the inflection point of the master curve. (b) Resulting bistable regime in the parameter plane of linker stiffness c and MT number M.

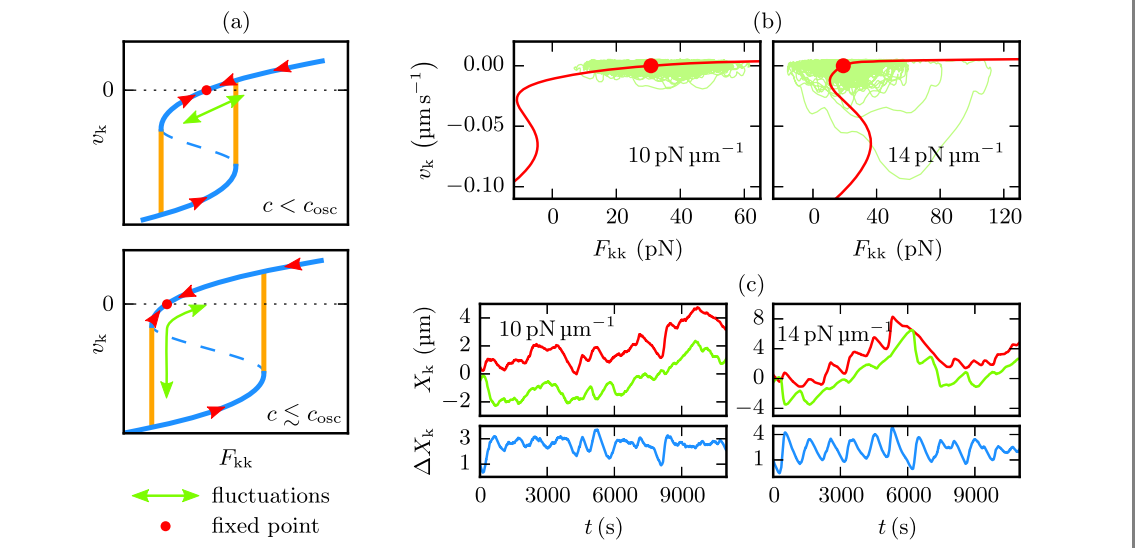

Figure 7. Kinetochore dynamics in the non-oscillatory regime. (a) Schematic explanation of kinetochore motion in the non-oscillatory regime based on the force–velocity relation. Where the upper branch crosses zero velocity, inter-kinetochore distance has a fixed point, around which it fluctuates. With higher linker stiffnesses c the fixed point comes closer to the left turning point $F_{\rm min}$. When c is just slightly smaller than $c_{\rm osc}$, fluctuations can be large enough for the kinetochore distance to leave the upper stable branch. Then, one of the two sister kinetochores passes once through the lower branch. (b) and (c) This behavior can be observed in simulations. While at $c = 10$ pN μm^{-1} kinetochores just fluctuate around the fixed point, at $c = 14$ pN μm^{-1} the kinetochores occasionally pass through the hysteresis loop. Simulations were performed with an unconfined system and 100 MTs on each side.

fixed point kinetochore motion will relax to zero velocity and just exhibit fluctuations around an equilibrium distance instead of oscillations.

As a sufficient condition for oscillations we have to require—besides bistability—a strictly positive velocity in the upper and a strictly negative velocity in the lower branch in the $v_{\rm k}$–$F_{\rm kk}$-diagram. Based on this condition we quantify an oscillatory regime in the parameter plane of linker stiffness c and MT number M in figure 8(a). In the limit of many MTs the sufficient condition for oscillations can be formulated in terms of the master curve: the maximum of the master curve has to be located at a positive and the minimum at a negative velocity. This is the case for $c > c_{\rm osc} = 15.91$ pN μm^{-1}, which is, therefore, a lower bound for the occurrence of oscillations. This constraint on the linker stiffness for metaphase chromosome oscillations provides additional information on MT–kinetochore linkers whose molecular nature is not known up to now.

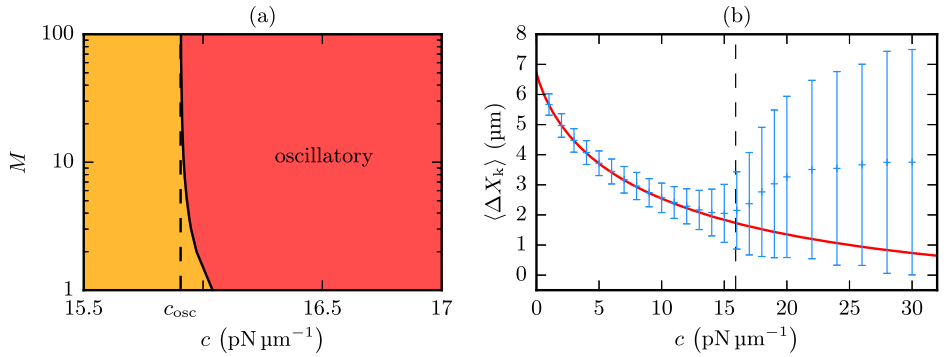

Figure 8. Constraints for oscillations in the two-sided model. (a) Oscillatory regime in the parameter plane of linker stiffness c and MT number M. (b) Mean inter-kinetochore distance according to (16) (red) and measured in simulations (blue) with $M = 100$. Below $c_{osc} = 15.91$ pN μm^{-1} (dashed line) both results match, whereas in the oscillatory regime mean inter-kinetochore distance diverges from the fixed point, and its standard deviation increases notably.

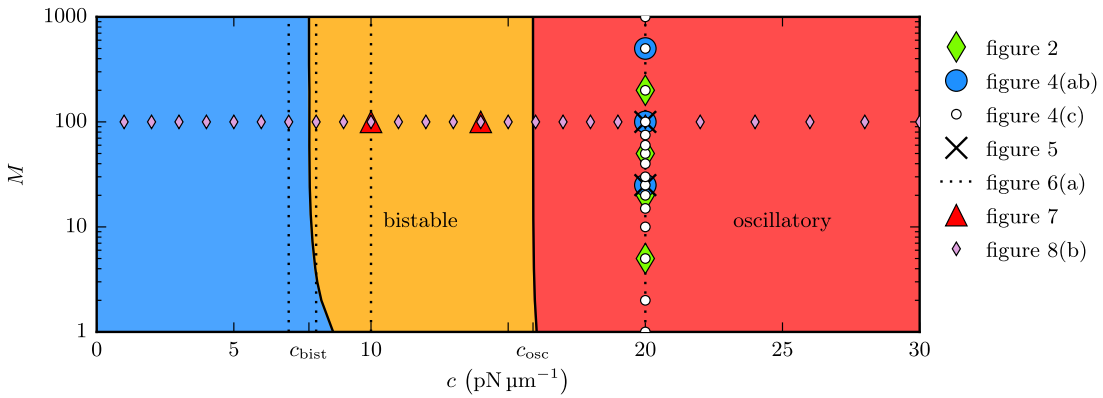

Figure 9. Locations in c–M-parameter plane of the master curves from figure 6(a) and the simulations from figures 2, 4, 5, 7 and 8.

Because of stochastic fluctuations, the transition between oscillatory and non-oscillatory regime is not sharp in our simulations. In the non-oscillatory regime kinetochores fluctuate around a fixed point of inter-kinetochore distance, where the upper branch crosses $v_k = 0$. However, these fluctuations can be large enough for the inter-kinetochore distance to shrink and leave the upper branch on the left side, especially for stiffnesses c slightly below c_{osc}. If that happens, one kinetochore passes once through the lower branch of the force–velocity relation just as in an oscillation. The difference to genuine oscillations is that these are randomly occurring single events (resulting in a Poisson process). Randomly occurring oscillations are visualized in figure 7 for $c < c_{osc}$ and $c \lesssim c_{osc}$. Moreover, the force–velocity relations as well as the kinetochore trajectories measured in corresponding simulations are shown.

In the non-oscillatory regime, the fixed point should determine the mean inter-kinetochore distance $\langle \Delta X_k \rangle = \langle X_{k,r} - X_{k,l} \rangle$. Solving the FPEs for $v_k = 0$, we compute the (external) force F_0 that has to be applied to one kinetochore to stall its motion:

$$F_0 = \gamma v_k - cM\langle x \rangle = -cM\langle x \rangle (v_k = 0). \tag{15}$$

In the two-sided model this force is applied to the kinetochores by the cohesin bond at the fixed point. With $F_{kk} = c_k(\Delta X_k - d_0)$ we compute the corresponding mean inter-kinetochore distance:

$$\langle \Delta X_k \rangle = \frac{F_0}{c_k} + d_0 = -\frac{cM}{c_k}\langle x \rangle (v_k = 0) + d_0. \tag{16}$$

Figure 8(b) shows that simulations agree with this result in the non-oscillatory regime. At c_{osc} the transition to the oscillatory regime can be recognized, where the mean inter-kinetochore distance deviates from the fixed point (16). Moreover, the variance of ΔX_k increases significantly at c_{osc} due to the transition to the oscillatory regime.

Table 4. Metaphase poleward flux velocities v_f and occurrence of directional instability. For a more detailed review of poleward flux measurements see [45].

Cell type	v_f (nm s^{-1})	Directional instability
LLC-PK1 (porcine)	8.3 [8]	Yes [8]
PtK1 (rat kangaroo)	7.7 [47]	Yes [11]
PtK2 (rat kangaroo)	10 [8]	Yes [12]
Newt lung	9.0 [48]	Yes [6]
U2OS (human)	8.8 [9]	Yes [9]
Drosophila embryo	32 [49]	No [13]
Xenopus egg	37 [50]	No [14]

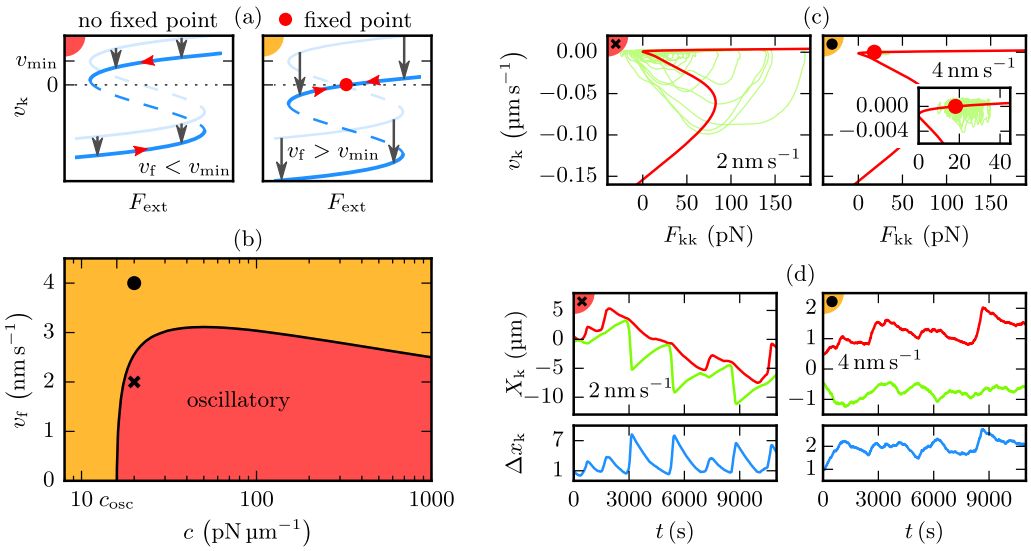

Figure 10. Poleward flux suppresses oscillations. (a) Due to (17), the force–velocity relation is shifted by the amount of the flux velocity v_f toward smaller kinetochore velocities. If the flux is slower than the kinetochore velocity v_{min} in the left turning point F_{min}, the kinetochores still oscillate. For larger flux velocities, a fixed point arises on the upper branch and the kinetochores behave as described in figure 7. (b) Oscillatory regime in the parameter plane of c and v_f in the limit of many MTs. Fast poleward flux suppresses kinetochore oscillations for arbitrary linker stiffnesses c. (c) and (d) Phase space diagrams and MT trajectories from simulations of the unconfined two-sided model with $c = 20$ pN μm^{-1} and $M = 100$. While at $v_f = 2$ nm s^{-1} the system is still in the oscillatory regime, where hysteresis is recognizable in phase space, at $v_f = 4$ nm s^{-1} kinetochores show fluctuative motion as described in figure 7.

In order to provide an overview and to make orientation easier for the reader, we summarize in figure 9 where the stochastic simulations from the last three sections and the master curves in figure 6(a) are located in the parameter plane of linker stiffness c and MT number M, and which regime they are part of.

6. Poleward microtubule flux suppresses oscillations

An effect we have not included so far is poleward MT flux, which was observed in several metazoan cells (table 4). It describes the constant flux of tubulin from the plus-ends toward the spindle pole and is probably driven by plus-end directed kinesin-5 motors pushing overlapping antiparallel MTs apart as well as kinesin-13 proteins that are located at the centrosome and depolymerize the MTs at their minus-ends [24]. During metaphase, spindle and MT length can be maintained by simultaneous polymerization at the plus-ends [45], which results in a behavior similar to treadmilling of MTs [46].

Poleward flux can be easily included in our model by subtracting a constant flux velocity v_f from the MT velocity. Then, the relative MT–kinetochore velocities (7) become

$$v_\pm(x) = v_\pm^0 \exp\left(-\frac{cx}{F_\pm}\right) - v_f - v_k. \tag{17}$$

Hence, the flux velocity can be treated as an offset to the constant kinetochore velocity in the solution of the stationary FPEs. The final effect is a shift of both the master curves and the force–velocity relations by v_f toward smaller kinetochore velocities v_k as shown in figure 10(a). If the shift is so large that the left turning

point $F_{\min}$ of the force–velocity hysteresis is located at a negative velocity, poleward flux suppresses directional instability because a fixed point emerges, and we expect similar behavior as for intermediate linker stiffnesses in the previous section (see figure 7). In the limit of many MTs, the maximum flux velocity that still allows directional instability is given by the velocity in the maximum of the master curve, which provides the boundary of the oscillatory regime in the parameter plane of linker stiffness c and poleward flux velocity v_f (figure 10(b)). Phase space diagrams (figure 10(c)) and kinetochore trajectories (figure 10(d)) from simulations with appropriate flux velocities confirm our arguments exhibiting similar behavior as for intermediate linker stiffnesses in figure 7. For small flux velocities the boundary of the oscillatory regime in figure 10(b) approaches our above result $c_{\text{osc}} = 15.91$ pN μm^{-1}. For increasing flux velocities the oscillatory regime shrinks, and its boundary has a maximum at $c \approx 50$ pN μm^{-1} with $v_f \approx 3.11$ nm s^{-1}. We conclude that kinetochore oscillations can be suppressed by moderate flux velocities independently of the linker stiffness.

Our theory also agrees with and explains simulation results in [20], where, for large flux velocities, suppression of kinetochore oscillations were observed but at the same time maintenance of bistability. Moreover, our results explain the experimentally observed correlation between flux velocity and directional instability. Kinetochore oscillations have been observed in the mitotic vertebrate cells listed in table 4 (LLC-PK1, PtK1/2, newt lung, U2OS) which have poleward flux velocities not exceeding 10 nm s^{-1}, whereas in the mitosis of a Drosophila embryo as well as in meiosis of a Xenopus egg, where flux velocities are three to four times higher, chromosomes do not exhibit directional instability.

7. Polar ejection forces provide an alternating oscillation pattern and chromosome alignment at the spindle equator

So far, we have not included polar ejection forces (PEFs). They originate from non-kinetochore MTs interacting with the chromosome arms and pushing them thereby toward the spindle equator, either through collisions with the chromosome arms or via chromokinesins [27], and provide additional pushing forces on kinetochores. Therefore, they can be included into the model by adding forces $F_{\text{PEF,r}}(x_{\text{k,r}})$ and $F_{\text{PEF,l}}(x_{\text{k,l}})$ acting on kinetochores, which depend on the *absolute* position of the kinetochores [19]. Due to the exponential length distribution of free MTs as well as the spherical geometry of the MT asters, the density of non-kinetochore MTs decreases monotonically with the distance from the spindle pole. Therefore, we assume that PEFs reach their maximum at the centrosome and vanish at the spindle equator (located at $x = 0$), where opposite PEFs compensate each other. This assumption is supported by the monotonic PEF distribution that has been measured *in vivo* by Ke *et al* [51]. Here, we will only discuss linearized PEFs

$$F_{\text{PEF,l}}(X_{\text{k,l}}) = -kX_{\text{k,l}}, \quad F_{\text{PEF,r}}(X_{\text{k,r}}) = kX_{\text{k,r}}, \tag{18}$$

where the spring constant k defines the strength of the forces, and the signs are chosen so that a positive force acts in AP-direction. We show in figure S3 in the supplementary material that other force distributions do not differ qualitatively in their influence on the kinetochore dynamics.

To determine kinetochore trajectories of the two-sided model in the presence of PEFs, we can start from the same force–velocity relations as for the basic one-sided model. In the presence of PEFs, the total forces $F_{\text{k,l}}$ and $F_{\text{k,r}}$ that act on the left and the right kinetochore in AP-direction depend on the absolute kinetochore positions $X_{\text{k,l}}$ and $X_{\text{k,r}}$:

$$F_{\text{k,l}} = F_{\text{kk}}(\Delta X_{\text{k}}) + F_{\text{PEF,l}}(X_{\text{k,l}}), \tag{19}$$

$$F_{\text{k,r}} = F_{\text{kk}}(\Delta X_{\text{k}}) + F_{\text{PEF,r}}(X_{\text{k,r}}). \tag{20}$$

We can investigate the motion of kinetochores in the full two-sided model again by using a phase space diagram; in the presence of PEFs we use a v_{k}–F_{k}-diagram with the total force F_{k} in AP-direction on the horizontal axis and the velocity v_{k} in AP-direction on the vertical axis. Because the total forces contain the external PEFs they are no longer related by action and reaction and, thus, the two kinetochores no longer have the same position on the F_{k}-axis, but they still remain close to each other on the F_{k}-axis as long as the cohesin bond is strong enough.

A kinetochore on the upper/lower branch moves in AP-/P-direction with $v_{\text{k}}^{\pm}(F_{\text{k}})$ if $v_{\text{k}}^{+} > 0$ ($v_{\text{k}}^{-} < 0$). A kinetochore on the upper AP-directed branch will relax its AP-directed PEFs, while a kinetochore on the lower P-directed branch will build up AP-directed PEFs. After a time of equilibration the kinetochores behave as described in figure 11. When one kinetochore changes its direction from P to AP (switches to the upper branch) the sister kinetochore, which was on the upper branch before, becomes the leading

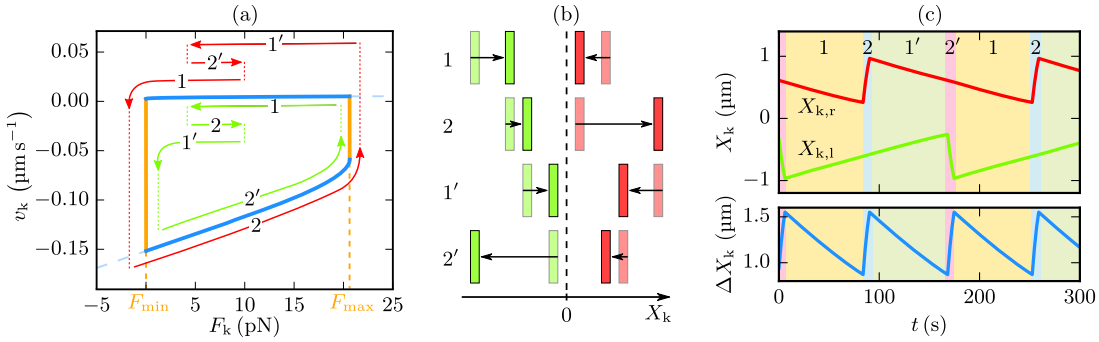

Figure 11. Kinetochore motion in the presence of PEFs. (a) and (b) At the beginning of state 1 the left kinetochore (green) has just switched from P- to AP-movement, so that both kinetochores are on the upper branch. Both kinetochores move in AP-direction, which means that both the cohesin force and the PEFs decrease and both kinetochores move left in the force–velocity diagram. Due to different PEFs, the right kinetochore (red) reaches the left turning point F_{min} first and switches to the lower branch, which marks the start of state 2. This state is dominated by the fast P-movement of the right kinetochore, which causes a steep increase of both F_{kk} and $F_{PEF,r}$. Therefore, the right kinetochore moves to the right in the force–velocity diagram. Meanwhile, the left sister still moves in AP-direction and $F_{k,l}$ increases slightly as the increase of F_{kk} is larger than the decrease of $F_{PEF,l}$. Since $\dot{F}_{k,r} > \dot{F}_{k,l}$, the right kinetochore overtakes its sister on the F_k-axis before it reaches the right turning point and switches to the upper branch. The then following states 1′ and 2′ are the exact opposite to 1 and 2 with swapped kinetochores. (c) Solution of the corresponding equations of motion for $c = 20$ pN μm^{-1}, $k = 10$ pN μm^{-1} and $M = 25$. For an animated version see video S4 in the supplementary material.

kinetochore (here, 'leading' refers to the position in the force velocity phase space). Therefore, the kinetochores do not reach the left turning point F_{min} at the same time so that it is always the leading kinetochore that switches to the lower branch. Since in general the absolute P-velocity is much larger than the AP-velocity ($-v_-$ for the lower branch is much larger than $+v_+$ for the upper branch), the AP-directed PEF contribution to the total force increases faster on the lower branch than on the upper one. As a result, the P-moving kinetochore overtakes its sister on the F_k-axis before switching back to the upper branch such that the leading kinetochore automatically becomes the trailing kinetochore in the next oscillation period (again, 'leading' and 'trailing' in terms of phase space positions). This periodic change of kinetochore positions in the force–velocity diagram leads to both regular breathing and regular single kinetochore oscillations, as the kinetochores alternately pass the lower branch. Solving appropriate equations of motions similar to (13) for each of the states depicted in figure 11(a) and (b), we determine the deterministic trajectories in figure 11(c) confirming this regular alternating oscillation pattern.

The alternating oscillation pattern robustly survives in stochastic simulations in the presence of moderate PEFs ($k \sim 10$ pN μm^{-1}) as we demonstrate in figure 12(a) by means of the kinetochore trajectories in real space. In figure 12(b), emergence of regular oscillations is illustrated in Fourier space: whereas for rather small values of k single kinetochore oscillations are still irregular resulting in a nearly monotonic decreasing Fourier transform, for $k = 10$ pN μm^{-1} single kinetochore motion has a distinct peak in the Fourier space indicating a regular shape of oscillations in real space. Moreover, frequency doubling of breathing compared to single kinetochore oscillations can directly be recognized by comparing the corresponding Fourier transforms. As a consequence of regular oscillations, the kinetochores stay near the spindle equator and cannot get stuck to one of the centrosomes as in the basic model, see histograms of kinetochore positions in figure 12(c). We conclude that PEFs are necessary to assure proper chromosome alignment in the metaphase plate at the spindle equator. This is consistent with an experiment by Levesque and Compton [52], who observed mitosis of vertebrate cells after suppressing the activity of chromokinesins and, thus PEFs. This resulted in 17.5% of the cells in at least one chromosome not aligning at the equator, but locating near a spindle pole.

Moreover, PEFs reduce the amplitude and increase the frequency of oscillations. The amplitude decreases for increasing PEF strength k as the kinetochores have to cover a smaller distance between the turning points at F_{min} and F_{max}. The increase of the frequency is linear in k, which can be deduced from the linear increase of $|\dot{F}_k|$:

$$|\dot{F}_{k,l}| = \left|c_k \left(v_{k,r} + v_{k,l}\right) + k v_{k,l}\right|, \tag{21}$$

$$|\dot{F}_{k,r}| = \left|c_k \left(v_{k,r} + v_{k,l}\right) + k v_{k,r}\right| \tag{22}$$

(defining $v_{k,l} \equiv \dot{X}_{k,l}$ and $v_{k,r} \equiv -\dot{X}_{k,r}$ as the velocities in AP-direction as before).

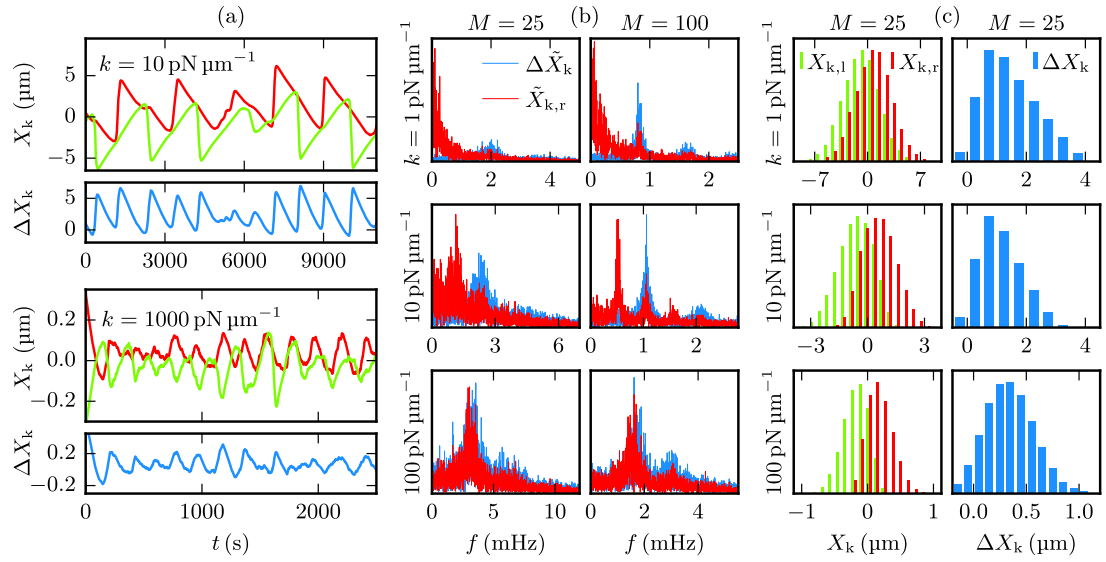

Figure 12. Kinetochore dynamics under the influence of PEFs. (a) Kinetochore trajectories with different PEF constants k from simulations with $M = 100$, $c = 20$ pN μm^{-1} and without confinement at the spindle poles. The PEFs force the kinetochores to oscillate regularly and to stay near the spindle equator. For $k = 10$ pN μm^{-1} kinetochores oscillate as described in figure 11. Since with strong PEFs kinetochores tend to switch to the lower branch simultaneously when reaching F_{min} in the phase space at the same time, for $k = 1000$ pN μm^{-1} oscillations are in antiphase due to symmetric initial conditions before the system equilibrates at $t \approx 1500$ s. After equilibration, periods of antiphase oscillations reappear over and over again due to fluctuations. Stronger PEFs cause a more fluctuative kinetochore motion. Especially for moderate MT numbers, this can lead to suppression of kinetochore oscillations. For animated versions of phase space trajectories see videos S5 ($k = 10$ pN μm^{-1}) and S6 ($k = 1000$ pN μm^{-1}) in the supplementary material. (b) Single (right) kinetochore and breathing oscillations in Fourier space. For weak PEFs ($k = 1$ pN μm^{-1}) single kinetochore oscillations are still irregular and $\tilde{X}_{k,r}$ has its maximum at $f = 0$. If $k = 10$ pN μm^{-1}, $\tilde{X}_{k,r}$ has a distinct peak at half the breathing frequency, indicating regular oscillations as described in figure 11 and frequency doubling of breathing compared to single kinetochore oscillations. With sufficiently strong PEFs ($k \gtrsim 100$ pN μm^{-1}) frequency doubling is lost as a consequence of antiphase oscillations and the peaks of $\tilde{X}_{k,r}$ and $\Delta\tilde{X}_k$ coincide with each other. (c) Histograms of kinetochore positions and inter-kinetochore distances for the realistic case of $M = 25$. Chromosomes are aligned at the spindle equator despite missing confinement at the centrosome. The range of kinetochore positions is narrower and the distances smaller if PEFs are stronger.

Since PEFs do not have any influence on the underlying master curves and force–velocity relations, they do not affect the kinetochore velocities v_k and never completely suppress kinetochore oscillations in the deterministic Fokker–Planck model, but only reduce their amplitude and increase their frequency. For strong PEFs, however, this gives rise to kinetochore motion with a fluctuative character, see figure 12 (see also video S6 in the supplementary material). The same observation was made in the model of Civelekoglu-Scholey *et al* [19]. Additionally, we detect sister kinetochore oscillations being in antiphase if PEFs are strong enough ($k \gtrsim 100$ pN μm^{-1}), see figure 12(a). This follows from the phase space velocities $\dot{F}_k$ being dominated by the strong PEFs compared to inter-kinetochore tension: imagine, both kinetochores are in the upper branch of the phase space and reach the turning point F_{min} at nearly the same time. When now one of the two kinetochores switches to the lower branch and starts moving polewards, its sister does not change its direction in phase space as in state $2/2'$ in figure 11(a) but continues moving left since the decrease of PEFs due to its poleward motion cannot be compensated by the increasing AP-directed cohesin tension if $k \gg c_k$. As a consequence, the kinetochore will switch to the lower branch just after its sister and both kinetochores pass the lower branch simultaneously, i.e. move apart from each other, finally resulting in antiphase oscillations. While the antiphase behavior vanishes after a certain time of equilibration in the deterministic model, in stochastic simulations periods of antiphase oscillations can be observed over and over again regardless of whether the system has been equilibrated before. A characteristic of antiphase oscillations is the loss of frequency doubling which also appears in the Fourier space where the peaks of single kinetochore and breathing motion coincide with each other if PEFs are strong, see figure 12(b). Since antiphase kinetochore oscillations have not been observed experimentally, we conclude that *in vivo* PEFs are weak compared to the inter-kinetochore tension but strong enough to assure chromosome alignment at the spindle equator. Compared to experimental results [6, 7, 10–12, 19], in our model, $k = 10$ pN μm^{-1} seems a reasonable choice as it assures regular oscillations with frequency doubling, keeps the inter-kinetochore distance within a suitable range of (1.2 ± 0.7) μm, and aligns kinetochores in a realistic maximum distance of 3 μm from the spindle equator with a standard deviation of 0.88 μm in the lifelike case of $M = 25$.

8. Catastrophe promotion at the kinetochore is required to stimulate directional instability if microtubules cannot exert pushing forces

So far, we assumed that MTs are also able to exert pushing forces on the kinetochore. During oscillations we find, on average, slightly less (48%) MT–kinetochore links under tension, while a substantial part of linkers also exerts pushing forces. Two experimental results suggest, however, that MTs do not directly exert pushing forces on the kinetochore: in [7], it was shown that the link between chromosomes is always under tension; the experiments in [26] demonstrated that, after removal of the cohesin bond, AP-moving kinetochores immediately stop indicating that kinetochore MTs cannot exert pushing forces, while P-moving kinetochores continue moving due to MT pulling forces.

In view of these experimental results and in order to answer the question whether MT pushing forces are essential for bistability and oscillations, we analyze variants of our basic model, where MT growth is confined at the kinetochore, i.e., where the relative coordinate $x = x_m - X_k$ is limited to $x \leqslant 0$ such that MTs can only exert tensile forces on the kinetochore. This implies that the kinetochore undergoes a catastrophe if it reaches the kinetochore, i.e., if the relative coordinate reaches $x = 0$ from below in the one-sided model. Different choices for the corresponding catastrophe rate ω_c^{kin} at $x = 0$ are possible: (i) a reflecting boundary, i.e., $\omega_c^{kin} = \infty$, where a catastrophe is immediately triggered if the MT plus-end reaches the kinetochore. (ii) A 'waiting' boundary condition, where the *relative* velocity $v_+ = v_{m+} - v_k = 0$ stalls if the MT reaches $x = 0$ (in the simulation, we set the MT velocity to $v_{m+} = v_k$). In contrast to the reflecting boundary condition, the catastrophe rate ω_c^{kin} at the kinetochore is finite such that the MT waits at the kinetochore until it undergoes a catastrophe for a mean waiting time $1/\omega_c^{kin}$, as similarly observed in metaphase of PtK1 cells [36]. Because $x = 0$ also results in $F_{mk} = 0$, the force-free catastrophe rate seems a natural choice, $\omega_c^{kin} = \omega_c^0$ [see (1)], which should be realized in the absence of any additional catastrophe regulating proteins at the centromere. (iii) If catastrophes are promoted by regulating proteins, but not immediately as for (i), we obtain intermediate cases of waiting boundary conditions with $\omega_c^0 < \omega_c^{kin} < \infty$. In mammalian cells, such regulating mechanisms could be provided by the kinesin MCAK, which is localized at the centromere during metaphase [53] and has been reported to increase the catastrophe rate of MTs roughly 7-fold [54]. Therefore, waiting boundary conditions with an increased catastrophe rate appear to be the most realistic scenario. We introduce a numerical catastrophe enhancement factor $n \geqslant 1$ characterizing the increased catastrophe rate, $\omega_c^{kin} = n\omega_c^0$. Within this general scenario reflecting boundary conditions (i) are recovered for $n = \infty$ and (ii) waiting boundary conditions with the zero force catastrophe rate for $n = 1$. We will discuss the general case (iii) in the following.

In our basic model, where MTs can exert pushing forces on kinetochores, the pushing phases where $x > 0$ can also be interpreted as a an effective waiting phase at the kinetochore with a catastrophe rate, which is effectively increased by the pushing forces. Therefore, the behavior of our basic model resembles a model with waiting boundary conditions with an increased catastrophe rate $n > 1$ at the kinetochore. MT pushing forces are not essential for bistability and oscillations and have a similar effect as an increased catastrophe rate at the kinetochore as our detailed analysis will show.

In the Fokker–Planck solution for the one-sided model, all confining boundary conditions limit the maximum MT–kinetochore distance x_{max} to zero, where it is positive in the basic model. When x_{max} is negative in the basic model (for $v_k > v_+^0$, see table 3), confining boundary conditions do not modify the basic model, since the MTs are not able to reach the fast kinetochore. For negative kinetochore velocities $v_k < v_-^0$, the minimum distance x_{min} becomes positive while x_{max} is zero. Then, all confining boundary conditions fix the MT tips to the kinetochore position as they do not shrink fast enough to move away from the poleward-moving kinetochore after a catastrophe resulting in $\langle x \rangle = 0$ and $F_{ext} = \gamma v_k$. All in all, confinement leads to the following maximal and minimal values for the MT–kinetochore distance x modifying table 3:

$$x_{max}^{conf} = \begin{cases} 0, & v_k < v_+^0 \\ x_{max}, & v_k \geqslant v_+^0, \end{cases} \qquad x_{min}^{conf} = \begin{cases} 0, & v_k < v_-^0 \\ x_{min}, & v_k \geqslant v_-^0. \end{cases} \tag{23}$$

We calculate the master curves $\langle x \rangle (v_k)$ for all three types of confining boundary conditions (see figure 13(a)). Because $x_{max}^{conf} \leqslant 0$ for any confining boundary condition, also $\langle x \rangle < 0$, i.e., the complete master curves lie in the regime of tensile MT–kinetochore linker forces reflecting the fact that pushing forces are strictly suppressed. Therefore, the MT–kinetochore catch bond is on average under tension establishing a more firm MT–kinetochore connection during the stochastic chromosome oscillations in metaphase. Oscillations then become a tug-of-war, in which both sets of MTs only exert pulling forces onto each other.

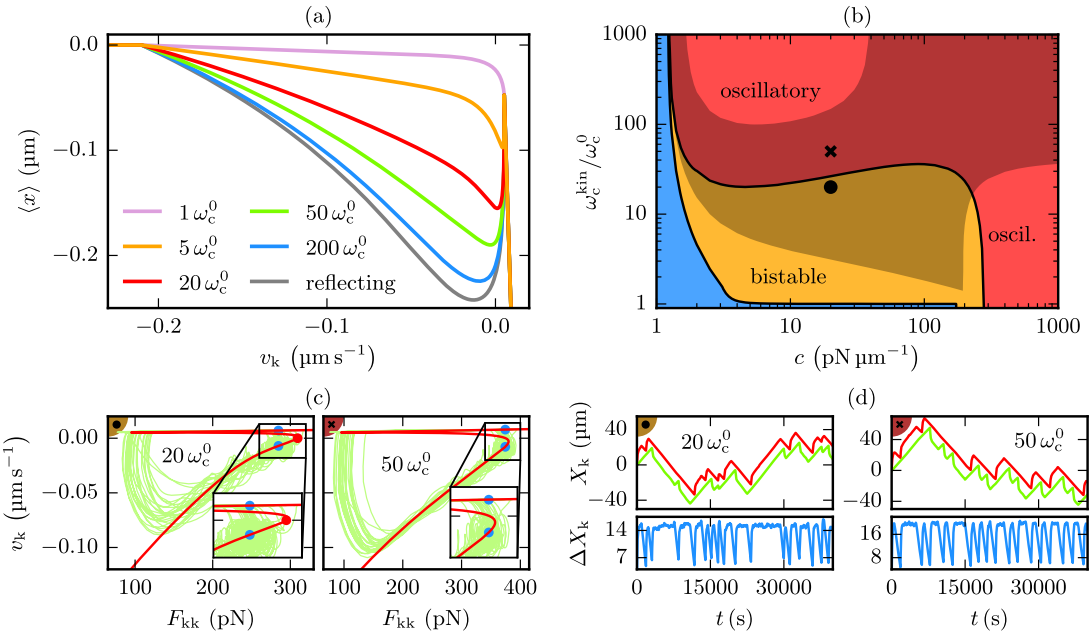

Figure 13. Microtubule confinement at the kinetochore. (a) Master curves of a system with a waiting boundary condition for various $\omega_c^{kin} = n\,\omega_c^0$ and $c = 20$ pN μm^{-1}. (b) Regimes in the parameter plane of c and ω_c^{kin} in the limit of many MTs. Outside the blue region, the master curve is bistable. In the orange region, the left branch of the master curve and, therefore, the lower branch of the v_k–F_{kk}-diagram cross $v_k = 0$, which leads to a fixed point suppressing oscillations (see text), whereas in the red region oscillations are possible. In stochastic simulations, kinetochores already oscillate at much smaller ω_c^{kin} than predicted by the master curves. Additionally, a new kind of fixed point, which is depicted in (c), emerges in the shaded region. (c) and (d) Phase space diagrams and kinetochore trajectories from simulations of the unconfined two-sided model with $c = 20$ pN μm^{-1} and $M = 100$. The blue dots mark the new kind of fixed point, where the leading kinetochore in the lower branch moves with the same velocity as the trailing kinetochore in the upper branch. Then the inter-kinetochore distance remains constant, while the center of mass moves with a constant velocity as in (d) for $\omega_c^{kin} = 20\,\omega_c^0$ at $t \approx 25\,000$ s. In the presence of PEFs, these fixed points are absent and the shaded region in (b) does not apply.

With a waiting boundary condition at the kinetochore, the probability densities $p_\pm(x, t)$ have to be supplemented with the probability $Q(t)$ to find an MT at the kinetochore ($x = 0$). Besides the FPEs (5) and (6) for the probability densities, we also have to solve the equation for the time evolution of $Q(t)$:

$$\partial_t Q(t) = v_+(0)p_+(0, t) - \omega_c^{kin} Q(t). \tag{24}$$

The analogous model for a free MT that grows against a rigid wall has already been solved in [41, 55]. In the stationary state, (24) leads to $Q = p_+(0)v_+(0)/\omega_c^{kin}$. For the probability densities $p_\pm(x)$ we get the same solution as for the basic model without confinement, except for the normalization constant. The overall probability density can then be written as $p(x) = p_+(x) + p_-(x) + Q\delta(x)$ and has to satisfy $\int_{x_{min}^{conf}}^{x_{max}^{conf}} p(x)\mathrm{d}x = 1$.

From the overall probability density $p(x)$ we obtain the master curves, which we show in figure 13(a) for $n = 1, 5, 20, 50, 200, \infty$ and a linker stiffness of $c = 20$ pN μm^{-1}. Again we can analyze the master curves for extrema to obtain constraints on linker stiffness c and catastrophe enhancement factor $n = \omega_c^{kin}/\omega_c^0$ for the occurrence of bistability and oscillations. The results of this analysis are shown in figure 13(b) as colored regions. It turns out that extrema in the master curve and, thus, bistability occur if the linker stiffness is sufficiently high $c > c_{bist}$. For the zero force catastrophe rate $n = 1$ we find a high threshold value $c_{bist} = 178$ pN μm^{-1}, in the limit of a reflecting boundary $n = \infty$ a very low threshold $c_{bist} = 1.218$ pN μm^{-1}.

We remind that a sufficient condition for oscillations is the absence of a stable fixed point, where one of the two branches in the v_k–F_{kk}-diagram crosses $v_k = 0$. In contrast to the basic model, the maxima of the master curve are now located at a positive velocity for $n > 1$. Therefore, oscillations are suppressed by a fixed point $v_k^- = 0$ on the lower branch in the v_k–F_{kk}-diagram, which occurs if the velocity is positive in the minimum of the master curve. In general, oscillations occur if the linker stiffness is sufficiently high $c > c_{osc}$. Again we find a high threshold value $c_{osc} = 280$ pN μm^{-1} for $n = 1$ and a low threshold $c_{osc} = 1.237$ pN μm^{-1} for a reflecting boundary condition ($n = \infty$).

For $n < 10$ the threshold values remain high. Moreover, at such high linker stiffnesses and for small n, the simulations of the two-sided model do not show the expected behavior. For $n = 1$ and high linker

stiffnesses in the oscillatory regime the kinetochore trajectories do not exhibit regular oscillations. Naively, one could argue that kinetochore oscillations are suppressed due to the lack of a pushing force and can be restored by additional PEFs. However, this is not the case, since, as stated above, PEFs do not affect the master curve that determines the regime of kinetochore motion. One reason for the absence of oscillations is that, for the zero force catastrophe rate ($n = 1$) the waiting time $1/\omega_c^{\mathrm{kin}} \sim 500\,\mathrm{s}$ (see table 2) at the kinetochore is large compared to the typical oscillation periods, which are in the range of 100–200 s.

Figure 13(b) also shows that oscillations require increased catastrophe rates with $n \gtrsim 20$ over a wide range of linker stiffnesses from $c = 10$ pN μm^{-1} to $c = 200$ pN μm^{-1}. For $n > 1$, at the boundary between bistable and oscillatory regime in figure 13(b), a fixed point $v_k^- = 0$ on the lower branch of the v_k–F_{kk} phase space diagrams appears, which can suppress oscillations. This fixed point is, however, less relevant because the kinetochores will only occasionally pass the lower branch simultaneously, which is necessary to reach this fixed point. Furthermore, this fixed point is located near the right turning point $F_{\max}$ so that the kinetochores can easily leave the fixed point by a stochastic fluctuation (as in figure 7). For these two reasons, in stochastic simulations, oscillations already occur for $n \gtrsim 5$, that is at a much lower n than the deterministically predicted $n \gtrsim 20$, but not for $n = 1$, i.e., in the absence of a catastrophe promoting mechanism.

The fixed point analysis of the v_k–F_{kk} phase space diagrams reveals that also a new type of fixed point corresponding to a non-oscillatory motion emerges for $n \lesssim 100$ in the shaded regions in figure 13(b). In this new type of fixed point, the leading P-moving kinetochore in the lower branch of the master curve has the same velocity as the trailing AP-moving kinetochore in the upper branch (see figure 13(c)) so that $\dot{F}_{kk} = -c_k\left(v_{k,r} + v_{k,l}\right) = 0$, and the inter-kinetochore distance remains constant, while the center of mass moves with a constant velocity (see figure 13(d)). In the presence of PEFs, however, this new type of fixed point does not survive because for the P-moving kinetochore the AP-directed PEFs increase, whereas they decrease for an AP-moving kinetochore. Then the upper blue dot in figure 13(c) moves to the left, while the lower blue point moves to the right such that this new type of fixed point is unstable in the presence of PEFs. Therefore, in the entire shaded region in figure 13(b) PEFs are essential to re-establish oscillations.

We conclude that both the linker stiffness $c > 10$ pN μm^{-1} and the catastrophe rate ω_c^{kin} at the kinetochore ($n \gtrsim 20$ or $n \gtrsim 5$ in the presence of stochastic fluctuations) have to be sufficiently large to obtain bistability and oscillations. Because additional catastrophe promoting proteins are necessary to increase the catastrophe rate at the kinetochore, the lowest values of n, which still enable oscillations, might be advantageous in the cellular system. We note that poleward flux can influence existence and positions of fixed points: an intermediate flow velocity can eliminate a fixed point on the lower branch by moving it into the unstable area of the phase space diagram. If flux is sufficiently large it can establish additional fixed points on the upper branch of the phase space diagrams, which suppress oscillations as in the basic model.

Moreover, the linker stiffness has to be sufficiently high to give linker extensions compatible with experimental results. An important part of the MT–kinetochore linkage is Ndc80, which is a rod-like fibril of total length around 60nm [56, 57] consisting of two coiled-coil regions with a flexible hinge that can adopt bending angles up to 120° with a broad distribution [57]. This bending corresponds to linker length changes of $|x| \sim 50$ nm. Moreover, fluorescent labeling showed total intra-kinetochore stretches around 100 nm [58] or 50 nm [12]. Therefore, we regard linker extensions $x \lesssim 100$ nm as realistic values. For large $n \gg 20$ only a small linker stiffness is necessary to enable oscillations. At the small threshold stiffness, the average linker length $|\langle x\rangle|$ is typically 1 μm in this regime. Increasing the linker stiffness leads to a decreasing linker length $|\langle x\rangle|$. We conclude that, for $n \gg 20$, experimental observations of linker extensions $|x| \lesssim 100$ nm put a stronger constraint on linker stiffness than the experimental observations of oscillations. Linker stiffnesses significantly above 5 pN μm^{-1} and, thus, far above c_{osc} are necessary to obtain a realistic linker length.

For $n \sim 10$–20, which is compatible with the experimental result $n \sim 7$ for the catastrophe promoter MCAK [54], and a linker stiffness $c = 20$ pN μm^{-1}, the increased catastrophe rate at the kinetochore leads to a realistic behavior with linker extensions $x \sim 100$ nm, which are also compatible with the experimental results [12, 56–58] (see figure 13(a)). This parameter regime is within the shaded regions in figure 13(b) and PEFs are necessary to establish oscillations. The linker extension is independent of PEFs.

For an increased catastrophe rate around $n \sim 10$–20 and a linker stiffness $c = 20$ pN μm^{-1}, the more realistic model with waiting boundary conditions at the kinetochore exhibits a similar behavior as our basic model because pushing phases where $x > 0$ in the basic model have a similar duration as waiting times at the kinetochore in the more realistic model.

9. Model parameters can be adjusted to reproduce kinetochore oscillations in PtK1 cells

So far, we took the experimentally measured parameters for MT transitions and velocities from table 2 for granted in order to analyze the effects of poleward flux, PEFs and confinement at the kinetochore by means of our mean-field theory. These values stem from experiments with yeast kinetochores [2], which can only bind one MT [59], whereas the mean-field theory is only correct if the kinetochores are attached to multiple MTs as in metazoan cells. Moreover, in budding yeast, the Ndc80 fibrils are connected to MTs via ring-like Dam1 complexes, which do not appear in metazoan cells [60]. In this section, we demonstrate that by adjusting the parameters of MT dynamics our model can reproduce experimental data of metazoan spindles using the example of PtK1 cells.

Our model exhibits a large difference of P versus AP-velocity (~ 100 vs ~ 4 nm s^{-1}, see figure 8) which is the origin of frequency doubling and also appears in PtK1 cells but not in this extent (~ 19 vs ~ 16 nm s^{-1}) [11]. As a consequence, in our model both kinetochores move toward each other in AP-direction (state 0 in figure 3) most of the time, whereas in the experiment, mostly one kinetochore moves in P-direction the trailing sister is moving in AP-direction (state $2/2'$ in figure 3). In a first step we will respect these results by adjusting the master curve (or force velocity relation) in a way that the two stable branches fit the experimentally measured velocities. This objective will be achieved by modifying the force-free MT velocities $v_\pm^0$ (shifting the upper/lower branch up- or downwards) and the corresponding characteristic forces $F_\pm$ (altering the slope of the upper/lower branch). Moreover, as a last parameter of MT dynamics, we will change the rescue rate ω_r^0 in order to adjust the MT–kinetochore distance to a realistic value. In a second step we will fit the measured frequencies and amplitudes by varying the parameters that do not affect the master curves (c_k, k).

Using the model with confinement at the kinetochore, we assume a ten times increased catastrophe rate $\omega_c^{kin} = 10\omega_c^0$ according to experimental results [54]. We set the linker stiffness to $c = 20$ pN μm^{-1} and keep it unchanged henceforth since this value results in strongly bistable master curves and the manifold consequences that a further modification of c has on kinetochore dynamics are hard to handle. The flux velocity is $v_f = 8$ nm s^{-1} (see table 4). The force-free MT growth velocity v_+^0 has to be greater than v_f for two reasons: firstly, detached MTs would not have a chance to reach the kinetochore again, otherwise. Secondly, this choice prevents a fixed point at the upper branch, as the left turning point in phase space (maximum of the master curve) is located at $v_+^0 - v_f$, when the MTs are confined at the kinetochore. We increase the force-free growth velocity roughly four-fold to $v_+^0 = 20$ nm s^{-1}, so that the minimum AP-velocity $v_+^0 - v_f = 12$ nm s^{-1} in the left turning point F_{min} lies below the observed mean velocity of ~ 16 nm s^{-1}. In order to adjust the maximum AP-velocity, we reduce the characteristic force in MT growth to $F_+ = 5$ pN, which leads to a steeper upper branch in the phase space diagram. The force-free shrinking velocity v_-^0 should be smaller than the observed P-velocity since the lower, P-directed branch always lies above it. Analogously to the upper branch and F_+, also the slope of the lower branch can be adjusted by varying the characteristic force F_-: an increase of F_-, i.e. a decrease of its absolute value, steepens the lower branch and thereby slows down the poleward motion. It turns out that it is a good choice to keep the values for v_-^0 and F_- from table 2 unchanged. Finally, we reduce the rescue rate ω_r^0, which lets MTs shrink to smaller lengths x_m (the minimum of the master curve is shifted downwards) and increases the MT–kinetochore distance $|x| = |X_k - x_m|$ to a realistic value.

Since we enable detachment in this section, we set $M = 35$ as it results in a mean number of ~ 20 attached MTs. Finally, we adjust the strength of PEFs k and the cohesin bond stiffness c_k to the following conditions: firstly, the PEFs have to be strong enough to assure proper chromosome alignment at the equator as well as a regular oscillation pattern, but should not dominate compared to the inter-kinetochore tension in order to prevent antiphase oscillations. Secondly, k and c_k affect the amplitude and the frequency of kinetochore oscillations which should resemble experimental results in the same manner: an increase of both k and c_k decreases the amplitude and increases the frequency. We find that $k = 20$ pN μm^{-1} and $c_k = 20$ pN μm^{-1} fulfill both conditions. In table 5, we list all parameters that we have changed compared to table 2.

The resulting kinetochore dynamics is shown in figure 14. The simulated kinetochore trajectories in figure 14(a) are very similar to the experimental results in [11, 19] as they exhibit frequency doubling of breathing compared to single kinetochore oscillations and move predominantly in phase, i.e. there is a leading P- and a trailing AP-kinetochore (state $2/2'$ in figure 3). The motion of the inter-kinetochore distance is rather fluctuative, resulting in a broad Fourier transform, in which the maximum at the breathing frequency is hardly recognizable, see figure 14(d). This is the only significant difference to the real kinetochore motion. The distributions of kinetochore positions as well as inter-kinetochore and MT–kinetochore distances (figures 14(e)–(g)) are in good agreement with experimental results [19].

Table 5. Parameters to reproduce of kinetochore oscillations in PtK1 cells. Parameters not listed here have been unchanged compared to table 2.

Description	Symbol	Value
Zero force rescue rate	ω_r^0	0.012 s^{-1}
Zero force MT growth velocity	v_+^0	20 nm s^{-1}
Characteristic force of MT growth	F_+	5 pN
Catastrophe rate at the kinetochore	ω_c^{kin}	0.019 s^{-1}
MT flux velocity	v_f	8 nm s^{-1}
PEF coefficient	k	20 pN μm^{-1}
Cohesin bond stiffness	c_k	20 pN μm^{-1}
MT–kinetochore linker stiffness	c	20 pN μm^{-1}
Number of MTs	M	35

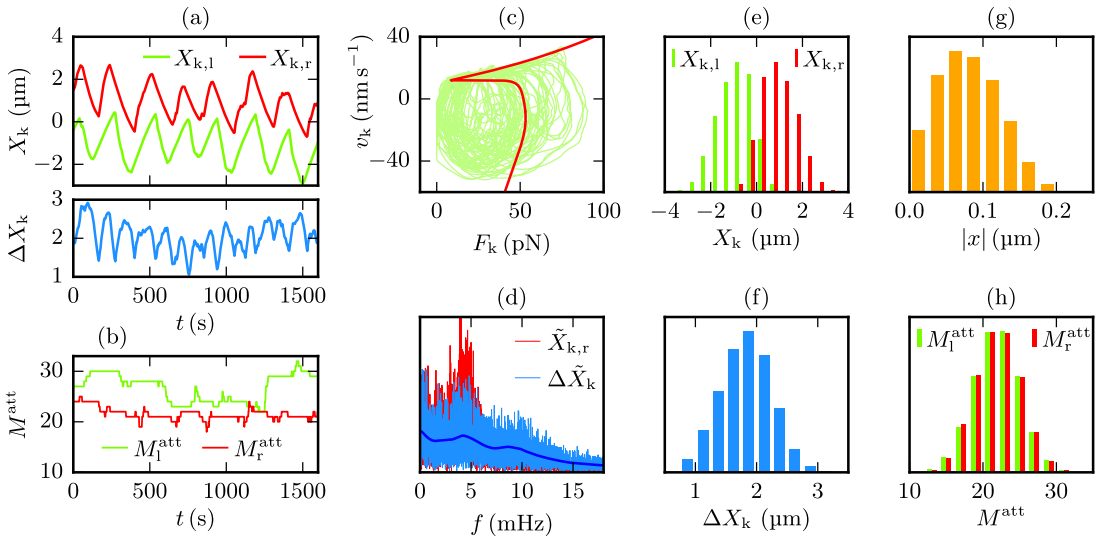

Figure 14. Reproduction of kinetochore oscillations in PtK1 cells. (a) Kinetochore positions and inter-kinetochore distance over time. Although the breathing oscillations are rather fluctuative, frequency doubling is recognizable. (b) Number of attached MTs over time. (c) Kinetochore motion in phase space (green) compared to the mean-field force–velocity relation (red, calculated with the mean number of attached MTs). For an animated version see video S7 in the supplementary material. (d) Position of the right kinetochore and inter-kinetochore distance in Fourier space. Fluctuative breathing oscillations lead to a Fourier transform with broad maxima, which are almost only recognizable in the smoothed curve (dark blue). (e)–(h) Distributions of kinetochore positions X_k, inter-kinetochore distance ΔX_k, MT–kinetochore distance $|x|$, and the number of attached MTs M^{att}.

Table 6. Characteristic quantities of model kinetochore oscillations compared to experimental results in PtK1 cells.

Description	Model	Experiment	
Mean P velocity	21.5 nm s^{-1}	19.0 nm s^{-1}	[11]
Mean AP velocity	15.7 nm s^{-1}	15.7 nm s^{-1}	[11]
Single kinetochore frequency	4.27 mHz	4.14–4.23 mHz	[11]
Breathing frequency	∼8.6 mHz	8.25 mHz	[11]
Mean inter-kinetochore distance	(1.83 ± 0.42) μm	(1.90 ± 0.44) μm	[19]
Mean MT–kinetochore distance	(0.081 ± 0.042) μm	(0.11 ± 0.04) μm	[19]
Standard deviation of kinetochore position	0.76 μm	0.5–1.1 μm	[19]
Mean number of attached MTs	21.4	20–25	[43]

In table 6, we list several characteristic quantities of kinetochore oscillations that have also been determined experimentally for PtK1 cells. Comparison with our model results shows quantitative agreement. In particular, the large discrepancy in the P- and AP-velocities is eliminated.

10. Discussion

We provided an analytical mean-field solution of the one-sided spindle model introduced by Banigan *et al* [20], which becomes exact in the limit of large MT numbers. The mean-field solution is based on the calculation of the mean linker extension $\langle x \rangle$ as a function of a constant kinetochore velocity v_k (the master

curve). Together with the equation of motion of the kinetochore we obtained the force–velocity relation of the one-sided model from the master curve. Our solution clearly shows that the force feedback of linkers onto the MT depolymerization dynamics is essential for a bistable force–velocity relation within the minimal model. The shape of the distribution $p_{\pm}(x)$ of linker lengths (12) is governed by this force feedback, and we traced the bistability to the peakedness (kurtosis) of this distribution.

Bistability of the force–velocity relation in the one-sided model is a necessary (but not sufficient) condition for oscillations in the two-sided model. Interpreting the bistable force–velocity relation as phase space diagram, we mathematically described kinetochore oscillations as an emergent result of collective dynamics of coupled MTs that exhibit dynamic instability individually. Our theory becomes exact in the limit of large MT numbers M. This interpretation of oscillations is underpinned by the experimental observations that kinetochore oscillations in budding yeast [61–63], where each kinetochore is attached to one MT [59], as well as in fission yeast [21, 64], where two to four MTs interact with the same kinetochore [65], have a considerably more fluctuative character than the regular oscillations in vertebrate cells [6–12] with ~ 20 MTs per kinetochore [43, 66]. Moreover, we were able to deduce idealized kinetochore oscillations, whose periods conform with experimental results [11]. For an MT–kinetochore linker stiffness $c = 20$ pN μm^{-1} and 20–25 MTs per kinetochore, we get periods of 206–258 s and 103–129 s for kinetochore and breathing oscillations, respectively. Our approach reproduced the frequency doubling of breathing compared to single kinetochore oscillations, observed in the experiment [11]. Both in the model and in the experiment this doubling originates from the different velocities of AP- and P-moving kinetochores, which ensure that a P-to-AP switch ($3/3'$ in figure 3) always follows an AP-to-P switch of the same kinetochore ($1/1'$ in figure 3). In the model the velocity difference is, however, much larger. As a consequence, in our model with 20–25 MTs an AP-to-P switch follows 96–119 s after a P-to-AP switch of the sister kinetochore, which is 93% of a breathing period, whereas in PtK2 cells a mean interval of merely 6 s has been measured [12]. In other words, in our model, most of the time both kinetochores move toward each other in AP-direction (state 0 in figure 3), whereas in the experiment, mostly one kinetochore moves in P-while the trailing sister is moving in AP-direction (state $2/2'$ in figure 3). In our model, different AP- and P-velocities are based on the fact that the MT shrinkage is much faster than growth. The model parameters for MT dynamics were taken from experimental measurements with yeast kinetochores [2], which, however, are distinct from metazoan kinetochores in two main points: firstly, they can only attach to one MT [59]; secondly, the Ndc80 fibrils are connected to MTs via ring-like Dam1 complexes, which do not appear in metazoan cells [60]. We show in section 9 that this discrepancy can be eliminated by adjusting some MT parameters and, moreover, the model can reproduce kinetochore oscillations in PtK1 cells quantitatively.

In experiments with HeLa cells Jaqaman *et al* [67] observed an increase of oscillation amplitudes and periods when they weakened the cohesin bond. In our model, a smaller cohesin stiffness c_{k} has the same two effects as the inter-kinetochore distance has to be larger to reach the turning points F_{min} and F_{max} of the hysteresis loop, and the phase space velocity $\dot{F}_{\mathrm{kk}} = c_{\mathrm{k}} \left(v_{\mathrm{k,r}} + v_{\mathrm{k,l}}\right)$ and, therefore, the frequencies are proportional to c_{k}.

Our analytical approach also allowed us to go beyond the results of [20] and quantify constraints on the linker stiffness c and the MT number for occurrence of bistability in the one-sided model and for the occurrence of oscillations in the full model. We found that bistability requires linker stiffnesses above $c_{\mathrm{bist}} \simeq 8$ pN μm^{-1}. Bistability is, however, not sufficient for oscillations. Our phase space interpretation showed that bistability only leads to directional instability if the two branches of the force–velocity relation are also separated by the zero velocity line. This condition quantifies the oscillatory regime in the parameter plane of c and M. We predict that oscillations should only be observable if the MT–kinetochore linker stiffness is above $c_{\mathrm{osc}} \simeq 16$ pN μm^{-1}. Our model can thus provide additional information on the MT–kinetochore linkers whose molecular nature is unknown up to now. Several Ndc80 fibrils, which cooperatively bind to the MT, are an important part of the MT–kinetochore link and the stiffness of this Ndc80 link has been determined recently using optical trap measurements [68]. These experiments found stiffnesses above $\sim$20 pN μm^{-1}, which are compatible with our bounds. Moreover, they found a stiffening of the link under force, which could be included in our model in future work.

The derivation of the lower bound for the stiffness for the occurrence of oscillations is based on the occurrence of a new zero AP-velocity fixed point in the force–velocity diagram of the kinetochores, which suppresses oscillations upon decreasing the stiffness. Also the influence of poleward flux to the system could be analyzed by a fixed point analysis of the force–velocity diagram. Since poleward MT flux shifts the force–velocity diagram toward smaller AP-velocities of the kinetochore, the upper branch may cross zero velocity establishing again a zero velocity fixed point suppressing oscillations. This explains why high flux velocities suppress directional instability and rationalizes the correlation between kinetochore oscillations and poleward flux observed in several cells (table 4). It has been observed in newt lung cells that oscillations

are occasionally (11% of time) interrupted by phases in which the kinetochores pause their motion [6] analogously to resting in the fixed point in our model. This indicates that the spindle of newt lung cells operates near the boundary between the oscillatory and the non-oscillatory regime.

Also experimental results in [69–72] on the effects of phosphorylation of Hec1, which is part of mammalian Ndc80 complex, onto kinetochore dynamics can be rationalized by our force–velocity diagram of the kinetochores. Dephosphorylation leads to hyper-stable MT–kinetochore attachments, increases the inter-kinetochore distance, damps or completely suppresses oscillations, and lets the kinetochores more often be found in a 'paused state'. The increase of the inter-kinetochore distance can be explained with the hyper-stable MT–kinetochore attachments: in the oscillatory regime, the bistable area of the force–velocity relation increases if more MTs are attached to the kinetochore (figure 2(b)); in the non-oscillatory regime, the mean distance $\langle \Delta X_k \rangle$ is a linear function of M ((16)). However, the suppression of oscillations and the frequent appearance of paused states, which are both effects of leaving the oscillatory regime in our model, cannot be explained with an increasing number of attached MTs. Instead, we suggest three additional effects of Hec1 phosphorylation: firstly, it is imaginable that Hec1 is a catastrophe factor that is activated by phosphorylation, i.e., if phosphorylation is suppressed, the catastrophe rate at the kinetochore ω_c^{kin} decreases. Secondly, phosphorylation of Hec1 could stiffen the Ndc80 complex so that dephosphorylation suppresses oscillations by decreasing the linker stiffness c. Since the stiffness of the Ndc80 complex has been measured in a recent experiment [68], this second option might be testable. The third possible explanation is based on the observation of Umbreit *et al* [73] that phosphorylation of Hec1 suppresses rescues. Following the argumentation in section 3, we conclude that an decreased rescue rate has a similar effect as an increase of the linker stiffness: since the exponent α_- that defines the leading order of $p(x)$ near x_{min} is a linear function of ω_r^0 ($\alpha_- + 1 \propto \omega_r^0$, see supplementary material), the probability density $p(x)$ becomes sharper for negative kinetochore velocities if rescue is suppressed, finally leading to a bistable master curve that allows for oscillations. In [71], besides suppression, Hec1 phosphorylation has also been enforced on up to four sites. As a result, the number of attached MTs and the periods of kinetochore oscillations decreased, which is consistent with our model (figure 4(c)). Moreover, kinetochore oscillations were supported but became more erratic just like in our model, where kinetochore motion is more fluctuative if less MTs are attached (figures 4(a) and (b)). This experimental result reinforces our point of view that regular kinetochore oscillations are an emergent phenomenon that results from the collective behavior of stochastic MT dynamics.

Furthermore, we added linearly distributed PEFs, which depend on the absolute kinetochore positions. Their main effect is a phase shift between the sister kinetochores in their phase space trajectories, which leads to regularly alternating kinetochore oscillations and, finally, forces the kinetochores to stay near the spindle equator. Consistently, experimental results show that a proper formation of the metaphase plate is not assured when PEFs are suppressed [52]. Since the PEFs do not affect the master curves and phase space diagrams, deterministically, they never completely suppress oscillations but only reduce their amplitude and increase their frequency, while the kinetochore velocities v_k are unchanged. This is consistent with experiments of Ke *et al* [51], who observed an increase in amplitude but no influence on the occurrence of oscillations and the velocity of chromosomes after severing the chromosome arms and thereby weakening the PEFs. In stochastic simulations, the kinetochore oscillations are more fluctuative in the presence of PEFs, see figure 12. A similar observation was made in the model of Civelekoglu-Scholey *et al* [19]. Moreover, in stochastic simulations, sister kinetochores tend to oscillate in antiphase and frequency doubling of breathing compared to single kinetochore oscillations is lost if PEFs are strong compared to the inter-kinetochore tension ($k \gg c_k$). Since to our knowledge such antiphase oscillations have not been observed *in vivo*, we conclude that the inter-kinetochore tension is the dominating force for directional instability.

Consistently with experimental observations in both fission yeast [74, 75] and human cells [76], kinesin-8 motors investigated in the model of Klemm *et al* [21] have a similar centering effect as the PEFs in our model. Since fission yeast does not contain chromokinesins [77], the Klemm model does not include PEFs, whereas our model does not include kinesin-8. It remains an open question whether and how the similar effects of PEFs and kinesin-8 cooperate if both are present. As kinesin-8 depolymerizes MTs in a length-dependent manner [78, 79], it could be included in our model by a catastrophe rate ω_c that depends on the MT length x_m, While such MT length-dependent catastrophe rates can easily be implemented in the stochastic simulations, they are difficult to include into our mean-field theory, which is based on solving the FPEs (5) and (6) in relative coordinates rather than absolute MT lengths.

Finally, we lifted the assumption that MTs are able to apply pushing forces on the kinetochores because experiments suggest that MTs only exert tensile forces [7, 26]. Therefore, we confined MT growth at the kinetochore by catastrophe-triggering boundary conditions. The catastrophe rate for an MT at the kinetochore ω_c^{kin} can, in principle, range from the force-free MT catastrophe rate ω_c^0, which is realistic in the

Table 7. Summary. Effect of an increase of the parameter in the first column on occurrence, frequency, and amplitude of kinetochore oscillations.

Parameter	Symbol	Occurrence	Frequency	Amplitude	Additional effects
Linker stiffness	c	Stimulation	Decrease	Increase	Decrease of inter-kinetochore distance in non-oscillatory regime
Poleward flux	v_f	Suppression	Decrease	None	
Polar ejection forces	k	None	Increase	Decrease	PEFs force kinetochores to oscillate alternately and to stay near the spindle equator
Catastrophe rate of stalled MTs	ω_c^{kin}	Stimulation	Decrease	Increase	
Cohesin bond stiffness	c_k	None	Increase	Decrease	
MT number	M	(Stimulation)	Decrease	Increase	

absence of any catastrophe promoting proteins up to infinity if a catastrophe is immediately triggered. In the presence of the centromere-associated regulating protein MCAK increased catastrophe rates $\omega_c^{kin} = 7\omega_c^0$ are expected [54]. We found that *both* the linker stiffness c *and* the catastrophe rate ω_c^{kin} at the kinetochore have to be sufficiently large to obtain bistability and oscillations. We find, in particular, that the force-free MT catastrophe rate is not sufficient to lead to oscillations, which shows that catastrophe-promoting proteins are essential to induce oscillations. In the presence of PEFs, oscillations can be recovered also for relatively small catastrophe rates: for $\omega_c^{kin}/\omega_c^0 \sim 5$, we found no oscillations in the absence of PEFs; for $\omega_c^{kin}/\omega_c^0 < 2$ we found no oscillations at all. Moreover, the linker stiffness has to be sufficiently high to give linker extensions below 100 nm compatible with experimental results [12, 56–58]. For $\omega_c^{kin}/\omega_c^0 = 20$ and a linker stiffness of $c = 20$ pN μm^{-1}, we found realistic behavior. Our results can explain experimental observations in [80], where PtK2-cells were observed under depletion of centromeric MCAK, which decreases ω_c^{kin}. Then, in accordance to our results (see figures 13(c) and (d)), the turning point F_{max} of the hysteresis loop decreases. As a result the oscillation frequency increases and the mean centromere stretch decreases, while the 'motility rates', i.e., the velocities do not change.

Kinetochore motion in the non-oscillatory regime can be described as fluctuations around a fixed point with constant inter-kinetochore distance. This is exactly the behavior of peripheral kinetochores in PtK1 cells [11, 19], while the central kinetochores do exhibit directional instability. Civelekoglu-Scholey *et al* [19] explained this dichotomy with different distributions of polar ejection forces in the center and the periphery of the metaphase plate. However, the model kinetochore trajectories in the presence of strong PEFs, which they declare to be representative for the motion of peripheral kinetochores (figure 6(C) in [19]), still have a regular oscillating shape with only a reduced amplitude and an increased frequency, in agreement with the results of our model in figure 12. The experimental trajectories for peripheral kinetochores from [11, 19], on the other hand, are very fluctuative, hardly show any regular oscillations, and are very similar to the trajectories in the non-oscillatory regime of our model. For a clear characterization of the experimentally measured motion of peripheral kinetochores as either stochastic fluctuations or regular oscillations its representation in Fourier space would be helpful as already provided for the central kinetochores by Wan *et al* [11] and as provided in figure 12 for our model. If the Fourier transforms do not have any distinct peaks, differences in PEFs are ruled out as a possible explanation for the dichotomy in PtK1 cells according to both our model and the one of Civelekoglu-Scholey *et al*.

Instead, our results suggest differences in linker stiffness or catastrophe promotion as reasons for the dichotomy. For instance, less Ndc80 complexes could participate in peripheral MT–kinetochore links resulting in reduced linker stiffness and non-oscillatory behavior. Also a non-uniform MCAK distribution that decreases radially toward the periphery of the metaphase plate could reduce ω_c^{kin} and suppress oscillations of peripheral kinetochores. Differences in poleward flux might be another possible explanation for the dichotomy according to our results. However, Cameron *et al* [81] observed that the flux velocities in PtK1 cells do not depend on the chromosome to which an MT is attached.

In conclusion, the minimal model can rationalize a number of experimental observations. Particularly interesting are constraints on the MT–kinetochore linker stiffness that are compatible with recent optical trap measurements [68]. The predicted responses to the most relevant parameter changes are summarized in table 7 and suggest further systematic perturbation experiments, for example, by promoting catastrophes at the kinetochore.

Acknowledgments

We acknowledge support by the Deutsche Forschungsgemeinschaft (grant No. KI 662/9-1). We also acknowledge financial support by Deutsche Forschungsgemeinschaft and TU Dortmund University within the funding programme Open Access Publishing.

References

[1] Dumont S and Mitchison T J 2009 *Curr. Biol.* **19** R749–61
[2] Akiyoshi B, Sarangapani K K, Powers A F, Nelson C R, Reichow S L, Arellano-Santoyo H, Gonen T, Ranish J A, Asbury C L and Biggins S 2010 *Nature* **468** 576
[3] Santaguida S and Musacchio A 2009 *EMBO J.* **28** 2511–31
[4] Joglekar A P and DeLuca J G 2009 *Curr. Biol.* **19** R404–7
[5] Sarangapani K K and Asbury C L 2014 *Trends Genet.* **30** 150–9
[6] Skibbens R V, Skeen V P and Salmon E 1993 *J. Cell Biol.* **122** 859–75
[7] Waters J C, Skibbens R V and Salmon E 1996 *J. Cell Sci.* **109** 2823–31
[8] Mitchison T 1989 *J. Cell Biol.* **109** 637–52
[9] Ganem N J, Upton K and Compton D A 2005 *Curr. Biol.* **15** 1827–32
[10] Magidson V, O'Connell C B, Lončarek J, Paul R, Mogilner A and Khodjakov A 2011 *Cell* **146** 555–67
[11] Wan X, Cimini D, Cameron L A and Salmon E 2012 *Mol. Biol. Cell* **23** 1035–46
[12] Dumont S, Salmon E and Mitchison T J 2012 *Science* **337** 355–8
[13] Maddox P, Desai A, Oegema K, Mitchison T J and Salmon E 2002 *Curr. Biol.* **12** 1670–4
[14] Desai A, Maddox P S, Mitchison T J and Salmon E 1998 *J. Cell Biol.* **141** 703–13
[15] Joglekar A P and Hunt A J 2002 *Biophys. J.* **83** 42–58
[16] Civelekoglu-Scholey G, Sharp D, Mogilner A and Scholey J 2006 *Biophys. J.* **90** 3966–82
[17] Shtylla B and Keener J P 2010 *J. Theor. Biol.* **263** 455–70
[18] Shtylla B and Keener J P 2011 *SIAM J. Appl. Math.* **71** 1821–48
[19] Civelekoglu-Scholey G, He B, Shen M, Wan X, Roscioli E, Bowden B and Cimini D 2013 *J. Cell Biol.* **201** 577–93
[20] Banigan E J, Chiou K K, Ballister E R, Mayo A M, Lampson M A and Liu A J 2015 *Proc. Natl Acad. Sci. USA* **112** 12699–704
[21] Klemm A H, Bosilj A, Glunčić M, Pavin N and Tolić I M 2018 *Mol. Biol. Cell* **29** 1332–45
[22] Vladimirou E, Harry E, Burroughs N and McAinsh A D 2011 *Chromosome Res.* **19** 409–21
[23] Civelekoglu-Scholey G and Cimini D 2014 *Interface Focus* **4** 20130073
[24] Kwok B H and Kapoor T M 2007 *Curr. Opin. Cell Biol.* **19** 36–42
[25] Mitchison T and Kirschner M 1984 *Nature* **312** 237–42
[26] Khodjakov A and Rieder C L 1996 *J. Cell Biol.* **135** 315–27
[27] Mazumdar M and Misteli T 2005 *Trends Cell Biol.* **15** 349–55
[28] Hill T L 1985 *Proc. Natl Acad. Sci. USA* **82** 4404–8
[29] Ghanti D, Patra S and Chowdhury D 2018 *Phys. Rev.* E **97** 052414
[30] O'Connell C B, Khodjakov A and McEwen B F 2012 *Curr. Opin. Cell Biol.* **24** 40–7
[31] McIntosh J R, Grishchuk E L, Morphew M K, Efremov A K, Zhudenkov K, Volkov V A, Cheeseman I M, Desai A, Mastronarde D N and Ataullakhanov F I 2008 *Cell* **135** 322–33
[32] Powers A F, Franck A D, Gestaut D R, Cooper J, Gracyzk B, Wei R R, Wordeman L, Davis T N and Asbury C L 2009 *Cell* **136** 865–75
[33] Keener J P and Shtylla B 2014 *Biophys. J.* **106** 998–1007
[34] Dong Y, Beldt K J V, Meng X, Khodjakov A and McEwen B F 2007 *Nat. Cell Biol.* **9** 516
[35] McIntosh J R, O'Toole E, Zhudenkov K, Morphew M, Schwartz C, Ataullakhanov F I and Grishchuk E L 2013 *J. Cell Biol.* **200** 459–74
[36] VandenBeldt K J, Barnard R M, Hergert P J, Meng X, Maiato H and McEwen B F 2006 *Curr. Biol.* **16** 1217–23
[37] Armond J W, Vladimirou E, Erent M, McAinsh A D and Burroughs N J 2015 *J. Cell Sci.* **128** 1991–2001
[38] Zelinski B and Kierfeld J 2013 *Phys. Rev.* E **87** 012703
[39] Verde F, Dogterom M, Stelzer E, Karsenti E and Leibler S 1992 *J. Cell Biol.* **118** 1097–108
[40] Dogterom M and Leibler S 1993 *Phys. Rev. Lett.* **70** 1347
[41] Zelinski B, Müller N and Kierfeld J 2012 *Phys. Rev.* E **86** 041918
[42] Zeitz M and Kierfeld J 2014 *Biophys. J.* **107** 2860–71
[43] McEwen B F, Heagle A B, Cassels G O, Buttle K F and Rieder C L 1997 *J. Cell Biol.* **137** 1567–80
[44] Gay G, Courtheoux T, Reyes C, Tournier S and Gachet Y 2012 *J. Cell Biol.* **196** 757–74
[45] Rogers G C, Rogers S L and Sharp D J 2005 *J. Cell Sci.* **118** 1105–16
[46] Margolis R L and Wilson L 1978 *Cell* **13** 1–8
[47] Zhai Y, Kronebusch P J and Borisy G G 1995 *J. Cell Biol.* **131** 721–34
[48] Mitchison T and Salmon E 1992 *J. Cell Biol.* **119** 569–82
[49] Brust-Mascher I and Scholey J M 2002 *Mol. Biol. Cell* **13** 3967–75
[50] Miyamoto D T, Perlman Z E, Burbank K S, Groen A C and Mitchison T J 2004 *J. Cell Biol.* **167** 813–8
[51] Ke K, Cheng J and Hunt A J 2009 *Curr. Biol.* **19** 807–15
[52] Levesque A A and Compton D A 2001 *J. Cell Biol.* **154** 1135–46
[53] Wordeman L and Mitchison T J 1995 *J. Cell Biol.* **128** 95–104
[54] Newton C N, Wagenbach M, Ovechkina Y, Wordeman L and Wilson L 2004 *FEBS Lett.* **572** 80–4
[55] Mulder B M 2012 *Phys. Rev.* E **86** 011902
[56] Wei R R, Sorger P K and Harrison S C 2005 *Proc. Natl Acad. Sci. USA* **102** 5363–7
[57] Wang H W, Long S, Ciferri C, Westermann S, Drubin D, Barnes G and Nogales E 2008 *J. Mol. Biol.* **383** 894–903
[58] Maresca T J and Salmon E D 2009 *J. Cell Biol.* **184** 373–81
[59] Winey M, Mamay C L, O'Toole E T, Mastronarde D N, Giddings T H, McDonald K L and McIntosh J R 1995 *J. Cell Biol.* **129** 1601–15
[60] Cheeseman I M 2014 *Cold Spring Harbor Perspect. Biol.* **6** a015826
[61] Straight A F, Marshall W F, Sedat J W and Murray A W 1997 *Science* **277** 574–8
[62] Pearson C G, Maddox P S, Salmon E and Bloom K 2001 *J. Cell Biol.* **152** 1255–66
[63] Sprague B L, Pearson C G, Maddox P S, Bloom K S, Salmon E and Odde D J 2003 *Biophys. J.* **84** 3529–46
[64] Nabeshima K, Nakagawa T, Straight A F, Murray A, Chikashige Y, Yamashita Y M, Hiraoka Y and Yanagida M 1998 *Mol. Biol. Cell* **9** 3211–25
[65] Ding R, McDonald K L and McIntosh J R 1993 *J. Cell Biol.* **120** 141–51

[66] McEwen B F, Chan G K, Zubrowski B, Savoian M S, Sauer M T and Yen T J 2001 *Mol. Biol. Cell* **12** 2776–89
[67] Jaqaman K *et al* 2010 *J. Cell Biol.* **188** 665–79
[68] Volkov V A, Huis in 't Veld P J, Dogterom M and Musacchio A 2018 *eLife* **7** e36764
[69] DeLuca J G, Gall W E, Ciferri C, Cimini D, Musacchio A and Salmon E 2006 *Cell* **127** 969–82
[70] DeLuca K F, Lens S M and DeLuca J G 2011 *J. Cell Sci.* **124** 622–34
[71] Zaytsev A V, Sundin L J, DeLuca K F, Grishchuk E L and DeLuca J G 2014 *J. Cell Biol.* **206** 45–59
[72] DeLuca K F, Meppelink A, Broad A J, Mick J E, Peersen O B, Pektas S, Lens S M and DeLuca J G 2018 *J. Cell Biol.* **217** 163–77
[73] Umbreit N T, Gestaut D R, Tien J F, Vollmar B S, Gonen T, Asbury C L and Davis T N 2012 *Proc. Natl Acad. Sci. USA* **109** 16113–8
[74] Mary H, Fouchard J, Gay G, Reyes C, Gauthier T, Gruget C, Pécréaux J, Tournier S and Gachet Y 2015 *J. Cell Sci.* **128** 3720–30
[75] Gergely Z R, Crapo A, Hough L E, McIntosh J R and Betterton M D 2016 *Mol. Biol. Cell* **27** 3490–514
[76] Mayr M I, Hümmer S, Bormann J, Grüner T, Adio S, Woehlke G and Mayer T U 2007 *Curr. Biol.* **17** 488–98
[77] Wood V *et al* 2002 *Nature* **415** 871–80
[78] Varga V, Helenius J, Tanaka K, Hyman A A, Tanaka T U and Howard J 2006 *Nat. Cell Biol.* **8** 957–62
[79] Varga V, Leduc C, Bormuth V, Diez S and Howard J 2009 *Cell* **138** 1174–83
[80] Kline-Smith S L, Khodjakov A, Hergert P and Walczak C E 2004 *Mol. Biol. Cell* **15** 1146–59
[81] Cameron L A, Yang G, Cimini D, Canman J C, Kisurina-Evgenieva O, Khodjakov A, Danuser G and Salmon E 2006 *J. Cell Biol.* **173** 173–9